Available online at www.keaipublishing.com/en/journals/journal-of-magnesium-and-alloys/

ScienceDirect

Journal of Magnesium and Alloys xxx (xxxx) xxx

www.elsevier.com/locate/jma

Full Length Article

Tailoring microstructure and mechanical properties of high-pressure die-cast Mg-RE-Gd alloys via trace Al additions

Lingyun Feng[a,*], Xixi Dong[b,*], Shihao Wang[c,d], Qing Cai[e], Hangbiao Mi[a], Wei Guo[a,*], Shouxun Ji[e,*]

[a] State Key Laboratory of Intelligent Manufacturing Equipment and Technology, School of Mechanical Science and Engineering, Huazhong University of Science and Technology, Wuhan, Hubei 430074, China
[b] College of Mechanical and Electrical Engineering, Nanjing University of Aeronautics and Astronautics, Nanjing 210016, China
[c] SuperSTEM Laboratory, SciTech Daresbury Campus, Daresbury WA4 4AD, UK
[d] School of Chemical and Process Engineering, University of Leeds, Leeds LS2 9JT, UK
[e] Brunel Centre for Advanced Solidification Technology (BCAST), Brunel University London, Uxbridge, Middlesex UB8 3PH, UK

Received 11 October 2025; received in revised form 16 January 2026; accepted 18 February 2026
Available online xxx

Abstract

A trade-off between strength and ductility often constrains the widespread application of high-pressure die-casting (HPDC) Mg-RE alloys. This study modulates the intermetallic compounds at the grain boundary (GB) in Mg-3.5RE-1.5Gd alloys through trace Al additions (0, 0.5, and 1.0 wt.%). Multiscale characterization and density functional theory (DFT) revealed a transition from metastable Mg_3RE (Al-free) to petal-like Al_2RE_3 (0.5Al), followed by the coexistence of blocky Al_2RE and striped $Al_{11}RE_3$ (1.0Al). As the Al content increases, the $Mg_{12}RE$ network remains the major phase, but its connectivity weakens. At room temperature (RT), yield strength (YS) decreases from 175 to 169 and 165 MPa, whereas ultimate tensile strength (UTS) increases from 180 to 200 and 205 MPa, and elongation (El) rises from 1.9% to 2.3% and 2.4%. At 250 °C, the El increased while both YS and UTS decreased. At 300 °C, the Al-containing alloy exhibited a comparatively high level of El, though this was lower than that observed in the Al-free alloy. This outcome is consistent with the weakened $Mg_{12}RE$ network connectivity. The fracture analysis revealed a mixed quasi-cleavage fracture with dimples at RT. At elevated temperatures, the predominant form of fracture is intergranular ductile fracture. DFT calculations confirm that Al-RE compounds exhibit more negative formation enthalpies and higher moduli than Mg-RE phases. However, the continuous $Mg_{12}RE$ framework phase provides superior GB pinning and load transfer capabilities. The present study elucidates the Al-mediated phase control mechanism, thus offering a viable alloy design pathway for the optimization of HPDC Mg-RE alloys.

Keywords: Magnesium alloys; Microstructures; Mechanical properties; DFT; Strengthening mechanisms.

1. Introduction

Magnesium (Mg) alloys have garnered significant attention in recent years due to their low density, high specific strength, and excellent castability, making them ideal candidates for lightweight applications in the automotive, aerospace, and electronics industries [1,2]. Among them, high-pressure die casting (HPDC) is widely used to fabricate complex components due to its high dimensional precision and production efficiency. However, the mainstream Mg-Al alloys used in engineering applications, such as AZ91 and AM60, suffer from severe performance degradation at elevated temperatures [3]. This issue is primarily attributed to the poor thermal stability of the main strengthening phase, $Mg_{17}Al_{12}$, which tends to coarsen and dissolve above 120 °C, weakening grain boundary (GB) cohesion and leading to premature failure [4,5].

Peer review under the responsibility of Chongqing University.
* Corresponding authors.
E-mail addresses: fenglingyun@hust.edu.cn (L. Feng), dongxixi@nuaa.edu.cn (X. Dong), weig@hust.edu.cn (W. Guo), shouxun.ji@brunel.ac.uk (S. Ji).

https://doi.org/10.1016/j.jma.2026.102023

Please cite this article as: L. Feng, X. Dong, S. Wang et al., Tailoring microstructure and mechanical properties of high-pressure die-cast Mg-RE-Gd alloys via trace Al additions, Journal of Magnesium and Alloys, https://doi.org/10.1016/j.jma.2026.102023

To address this issue, recent studies have shifted toward binary and ternary magnesium-rare earth (Mg-RE) alloy systems, such as Mg-La [6], Mg-Nd [6,7], Mg-Gd [8,9], Mg-La-Gd [10], Mg-Nd-Gd [11], and Mg-Gd-Y [12,13]. These alloys form high-melting, thermally stable intermetallics such as $Mg_{12}RE$, Mg_3RE, and Mg_5RE, which inhibit GB migration and dislocation motion, thereby improving creep resistance and thermal stability [14]. In particular, the $Mg_{12}RE$ continuous eutectic network has been demonstrated to play a crucial role in enhancing the strength of Mg-RE alloys at both room and elevated temperatures [15,16]. However, these alloys face persistent challenges in HPDC applications, including low ductility, poor melt fluidity, and inadequate feeding during solidification [17,18]. This trade-off between thermal stability and castability remains a key obstacle to large-scale industrial deployment.

To mitigate these limitations, alloying strategies have been proposed to enhance the overall performance of Mg-RE alloys. Elements such as Zn [19,20], Mn [21], Si [22], and Sn [23] have been shown to contribute to solid solution strengthening, grain refinement, or modulation of eutectic formation [24]. Among these, Zn has attracted substantial interest due to its ability to induce the formation of long-period stacking ordered (LPSO) structures when combined with heavy rare earth elements (Gd, Y) [12,25]. These LPSO phases exhibit high fault densities and strong strain accommodation, offering outstanding strength-ductility synergy in thermomechanically processed states [26]. However, the formation of LPSO structures is sensitive to the Zn/RE ratio, cooling rate, and RE content, making them challenging to form under rapid solidification conditions, such as HPDC [26–28]. Additionally, high Zn content tends to form low-stability phases such as MgZn and $MgZn_2$ at high temperatures and exhibits significant segregation tendencies.

In this context, aluminum (Al) has emerged as a promising alloying element in Mg-RE alloy systems [29–31]. Al has been shown to enhance the melt flowability and mold filling capability of the alloy, thereby improving the manufacturability of HPDC processes [32]. Furthermore, Al exhibits strong chemical affinity with RE elements and readily forms a series of high-melting-point, thermodynamically stable intermetallic compounds during early solidification, such as Al_2RE and $Al_{11}RE_3$ [33]. Several commercial Mg-Al-RE alloys, such as AE42 and AE44, employ a comparatively elevated Al content to enhance formability while improving intermediate-temperature performance [34–36]. Nevertheless, a high Al content may also result in the formation of coarse intermetallic phases, grain coarsening, or even solidification cracks, which can lead to embrittlement [37]. Therefore, recent microstructure designs have placed a mounting emphasis on minimizing aluminum content, with a view to enhancing the overall strength, ductility, and thermal stability properties of HPDC alloys. Rong et al. [38] validated through research on HPDC Mg-3RE-0.5Zn-xAl ultra-thin-walled components that the addition of 1 wt.% and 2 wt.% Al promotes the transformation of the $Mg_{12}RE$ phase into the Al-RE phase, significantly enhancing the balance between strength and ductility. Zhao et al. [39] found that adding <2 wt.% Al to Mg-4l-xAl-0.5Mn does not improve strength-ductility, but instead reduces it. Our previous study [40,41] on HPDC Mg-3.5RE-1.5Gd-0.5Al-0.3Mn revealed the formation of a thermally stable Al_2RE_3 phase, contributing to its high-temperature creep performance. However, extant studies have primarily focused on macro-performance evaluations, lacking a mechanistic understanding of the evolution of Al-RE phases and their microstructural functions under low Al content additions. The mechanisms by which Al induces phase control and contributes to mechanical strengthening under HPDC conditions are not yet fully elucidated. Moreover, there is a lack of clear theoretical guidance on the formation priority, morphological evolution, and competitive behavior of Al-RE and Mg-RE phases. The dearth of comprehensive studies that integrate first-principles thermodynamic calculations with microstructural characterization further hinders the rational design and performance prediction of new high-temperature Mg alloys.

In light of these observations, the present study endeavors to methodically examine the impact of trace aluminum incorporation (0, 0.5, and 1.0 wt.%) on the microstructural evolution and high-temperature mechanical properties of HPDC Mg-3.5RE-1.5Gd alloys. Various analytical techniques, including XRD, SEM, EBSD, and TEM, were employed to elucidate the multiscale microstructure and phase distribution. Density Functional Theory (DFT) calculations were utilized to assess the formation enthalpies and elastic constants of representative Al-RE and Mg-RE phases. The present study integrates theoretical analysis with experimental observations to elucidate the intrinsic mechanism of Al-induced phase transformations and their contribution to the enhancement of high-temperature mechanical properties. This integration provides a scientific basis for designing strategies for developing next-generation high-performance HPDC Mg-RE alloys.

2. Experimental

2.1. Preparation of alloy melts and HPDC

The Mg-3.5RE-xGd-yAl alloys were prepared from high-purity raw materials: pure Mg (99.9 wt.%), pure Al (99.9 wt.%), pure Zn (99.9 wt.%), and master alloys of Mg-5 wt.% Mn, Mg-30 wt.% La, Mg-25 wt.% Ce, Mg-30 wt.% Nd, and Mg-30 wt.% Gd. The alloys were melted in an electric resistance furnace at 720 °C under a protective atmosphere of N_2 mixed with 0.5% SF_6 to prevent oxidation. The melt was held at 720 °C for 30 min with gentle mechanical stirring to ensure compositional homogeneity and to remove oxide films and inclusions. Following homogenization, mushroom-shaped samples were extracted for chemical analysis via Inductively Coupled Plasma-Optical Emission Spectrometry (ICP-OES). The measured chemical compositions of the investigated alloys are listed in Table 1.

High-pressure die casting was performed using a 4500 kN cold chamber die casting machine. The melt was manually poured into the shot sleeve at a temperature of 715 ± 5 °C, monitored by a calibrated type K thermocouple. The crit-

Please cite this article as: L. Feng, X. Dong, S. Wang et al., Tailoring microstructure and mechanical properties of high-pressure die-cast Mg-RE-Gd alloys via trace Al additions, Journal of Magnesium and Alloys, https://doi.org/10.1016/j.jma.2026.102023

Table 1
Chemical composition of experimental HPDC Mg-3.5RE-1.5Gd-xAl alloys (x = 0, 0.5, 1) obtained by ICP-OES.

Alloys	Code	La	Ce	Nd	Gd	Al	Zn	Mn	Mg
Mg-3.5RE-1.5Gd-0Al	EV42	1.57	0.98	0.93	1.44	-	0.49	0.27	Bal.
Mg-3.5RE-1.5Gd-0.5Al	EVA421A	1.62	0.95	0.94	1.51	0.46	0.46	0.26	Bal.
Mg-3.5RE-1.5Gd-1Al	EVA421B	1.61	1.03	1.01	1.46	0.96	0.52	0.30	Bal.

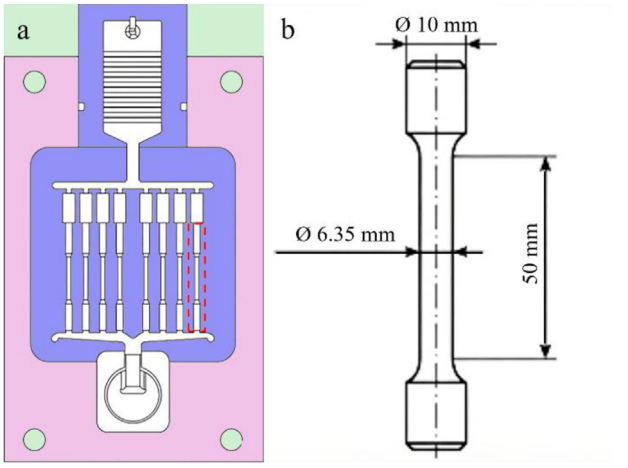

Fig. 1. (a) Schematic diagram of a die for forming tensile test specimens; (b) Schematic diagram of specimen dimensions for tensile testing.

ical processing parameters were meticulously controlled: a plunger injection speed of 3.0 m/s, an intensification pressure of 320 bar, and a mold temperature of 180 ± 5 °C. Eight tensile bars were produced per die-casting shot for each alloy composition to ensure statistical reliability, shown in Fig. 1a.

2.2. Tensile tests

Fig. 1b shows that tensile specimens with a gauge diameter of 6.35 mm and a gauge length of 50 mm were machined from the HPDC samples according to ASTM E8/E8M-16 and ASTM E21–20 standards. Tensile tests were conducted on an Instron 5500 universal testing machine with a 50 kN load cell. Room temperature (RT) tests were performed at a constant displacement rate of 1 mm/min. Strain was measured directly using a 50 mm gauge-length extensometer. Elevated-temperature tests at 250 °C and 300 °C were conducted inside a high-precision temperature-controlled chamber. Specimens were preheated and held at the target temperature for at least 15 min to ensure a uniform thermal distribution. Tests were performed at a constant displacement rate of 0.0002/s. Due to the risk of thermal damage, the percentage elongation after fracture was determined by carefully fitting the broken ends together after cooling to RT and measuring the final gauge length. In this study, elongation refers to the total elongation to fracture, which by definition includes both elastic and plastic components. A minimum of six valid tests were conducted for each alloy and temperature condition to obtain the average mechanical properties along with their standard deviations.

2.3. Microstructure analysis

Microstructural analysis was performed on samples sectioned from the center gauge length of the tested tensile specimens. Samples were mechanically ground with SiC abrasive papers up to 4000 grit and polished with diamond down to 1 μm. A polarized optical microscope (OM) was used with a Zeiss Axioscope. Scanning Electron Microscopy (SEM) and Energy-Dispersive X-ray Spectroscopy (EDX) were conducted using a ZEISS SUPRA 35VP field-emission microscope operated at 20 kV in backscattered electron (BSE) mode. The volume fraction of intermetallic phases was quantified using ImageJ software based on at least five low-magnification BSE images per condition. Electron Backscatter Diffraction (EBSD) analysis was performed using a TSL OIM system integrated into the SEM. Samples were electrolytically polished using a chilled solution of 12.6 g picric acid, 30 mL acetic acid, 30 mL water, and 420 mL ethanol at −30 °C and 20 V for 20–40 s. A step size of 0.8 μm was used for high-resolution mapping. Grain size statistics were derived using TSL OIM Analysis software. Transmission Electron Microscopy (TEM) foils were prepared by mechanical grinding to ∼50 μm, followed by ion-beam thinning using a Gatan PIPS system (3–5 kV, 3–5°). TEM characterizations, including bright-field (BF), high-angle annular dark-field scanning TEM (HAADF-STEM), high-resolution TEM (HRTEM), and selected-area electron diffraction (SAED), were conducted using a JEOL 2100F TEM operating at 200 kV. X-ray Diffraction (XRD) was carried out on a Bruker D8 Advance diffractometer with Cu Kα radiation. Scans were recorded over a 2θ range of 20° to 100° with a step size of 0.02° and a dwell time of 1 s per step for phase identification.

2.4. First-principles calculation methods

Density functional theory (DFT) calculations were performed using the Vienna Ab initio Simulation Package (VASP) to assess the thermodynamic stability and mechanical properties of key intermetallic phases. The exchange-correlation interaction was described by the generalized gradient approximation (GGA) with the Perdew-Burke-Ernzerhof (PBE) functional, and electron-ion interactions were treated with the projector augmented wave (PAW) method. As demonstrated in Fig. 2, the following structure data were employed for the first-principles calculation, based on the collected crystal structures of intermediate phases of the alloys in this research.

The purpose of conducting DFT calculations in this work is to elucidate the thermodynamic stability and fundamental

Please cite this article as: L. Feng, X. Dong, S. Wang et al., Tailoring microstructure and mechanical properties of high-pressure die-cast Mg-RE-Gd alloys via trace Al additions, Journal of Magnesium and Alloys, https://doi.org/10.1016/j.jma.2026.102023

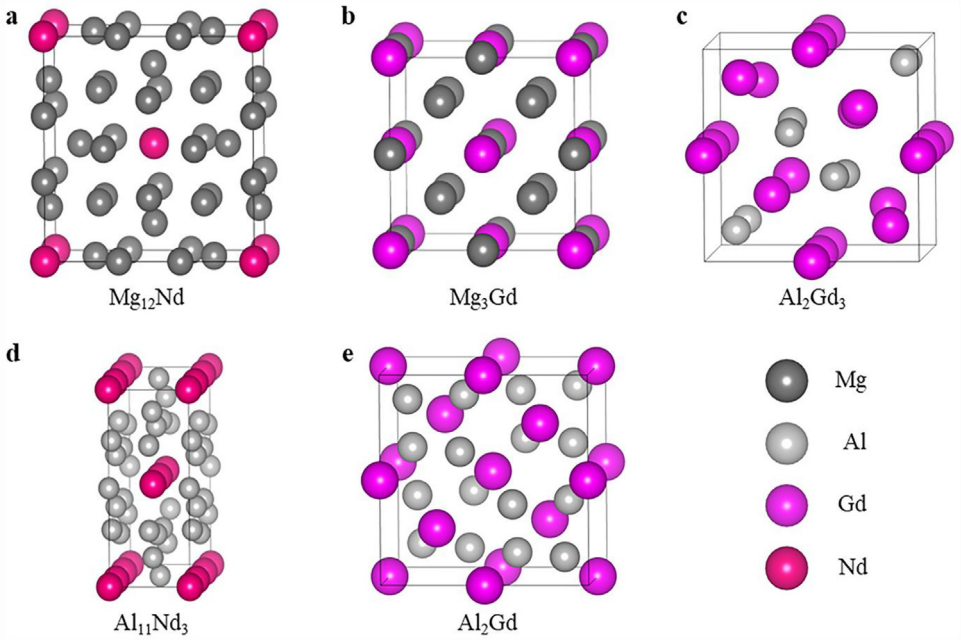

Fig. 2. Atomic models of the $Mg_{12}Nd$, Mg_3Gd, Al_2Gd_3, $Al_{11}Nd_3$ and Al_2Gd phases. (a–e) displays 3D views of the phases, respectively. Atoms are color-coded by species and their positions.

mechanical properties of key intermetallic compounds at the atomic scale. Based on existing literature and typical phase formation behavior in this alloy system, $Mg_{12}RE$, Mg_3RE, Al_2RE_3, $Al_{11}RE_3$, and Al_2RE are identified as the predominant intermetallic phases in the as-cast microstructure. To systematically evaluate the effect of Al addition on the intrinsic properties of these phases, representative structural models were constructed focusing on the key RE elements Gd and Nd. Accordingly, Mg_3Gd, $Mg_{12}Nd$, Al_2Gd_3, Al_2Gd, and $Al_{11}Nd_3$ were selected as simplified yet physically meaningful endpoint models for the DFT simulations.

All structures were fully relaxed until the total energy converged to within 10^{-6} eV/atom and the Hellmann-Feynman forces on each atom were <0.01 eV/Å. A plane-wave kinetic energy cutoff of 520 eV was employed. Monkhorst-Pack k-point meshes were tailored to each unit cell to ensure energy convergence within 1 meV/atom. The formation enthalpy, ΔH_f, was calculated using the following Eq. (1).

$$\Delta H_f = \frac{(E_{tot} - N_A E^A_{solid} - N_B E^B_{solid})}{(N_A + N_B)} \quad (1)$$

where E_{tot} is the total energy of the compound, N_A and N_B are the number of atoms, and E_{solid} is the energy of a single element.

Elastic stiffness constants (C_{ij}) were calculated by applying minor strains to the equilibrium structure and fitting the resulting stress-strain relationships. The bulk modulus (B), shear modulus (G), Young's modulus (E), and Poisson's ratio (ν) for polycrystalline aggregates were then derived from the C_{ij} values using the Voigt-Reuss-Hill (VRH) averaging scheme in Eqs. (2–9). The C_{ij} are the second-order single-crystal elastic stiffness constants in Voigt notation (in GPa), and S_{ij} are the corresponding elastic compliance constant defined as the elements of the inverse matrix of C_{ij} ($S = C^{-1}$). Subscripts V and R denote the Voigt and Reuss bounds, respectively, and the Hill average is obtained as B_{VRH} and G_{VRH}. In Eqs. (8–9), B and G refer to the Hill-average values B_{VRH} and G_{VRH}, from which E and ν are calculated for the polycrystalline aggregate. The mechanical stability of each phase was verified by checking the corresponding Born stability criteria shown in Table 2.

Table 2
Mechanical stability criteria of cubic, tetragonal and orthorhombic.

Structure	Mechanical stability criteria
Cubic	$C_{11}>0,\ C_{44}>0,\ C_{11}-C_{12}>0,\ C_{11}+2C_{12}>0$
Tetragonal	$C_{11}>\lvert C_{12}\rvert,\ 2C_{13}^2<C_{33}(C_{11}+C_{12}),\ C_{44}>0,\ C_{66}>0$
Orthorhombic	$C_{11}>0,\ C_{22}>0,\ C_{33}>0,\ C_{44}>0,\ C_{55}>0,\ C_{66}>0,$ $C_{11}+C_{22}+C_{33}+2(C_{12}+C_{13}+C_{23})>0,$ $C_{11}+C_{22}-2C_{12}>0,\ C_{11}+C_{33}-2C_{13}>0,$ $C_{22}+C_{33}-2C_{23}>0$

$$Bv = \frac{1}{9}(C_{11}+C_{22}+C_{33}+2C_{12}+2C_{13}+2C_{23}) \quad (2)$$

$$Gv = \frac{1}{15}(C_{11}+C_{22}+C_{33}-C_{12}-C_{13}-C_{23}) + \frac{1}{5}(C_{44}+C_{55}+C_{66}) \quad (3)$$

$$B_R = \frac{1}{(S_{11}+S_{22}+S_{33})+2(S_{12}+S_{23}+S_{31})} \quad (4)$$

$$G_R = \frac{15}{4(S_{11}+S_{22}+S_{33})-(S_{12}+S_{13}+S_{23})+3(S_{44}+S_{55}+S_{66})} \quad (5)$$

$$G_{VRH} = \frac{G_V + G_R}{2} \quad (6)$$

Please cite this article as: L. Feng, X. Dong, S. Wang et al., Tailoring microstructure and mechanical properties of high-pressure die-cast Mg-RE-Gd alloys via trace Al additions, Journal of Magnesium and Alloys, https://doi.org/10.1016/j.jma.2026.102023

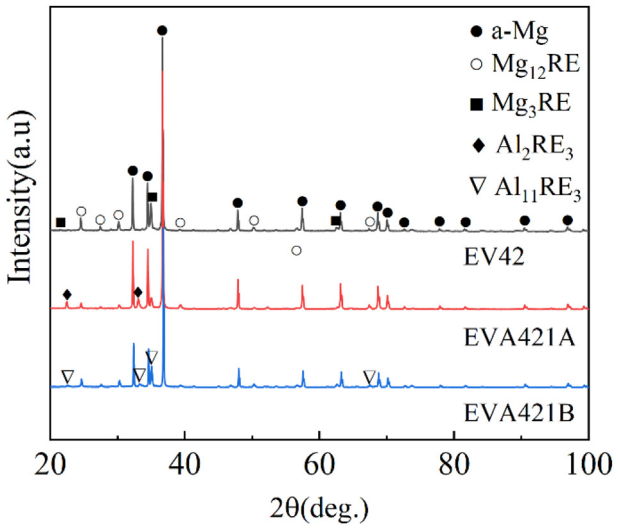

Fig. 3. X-ray diffraction (XRD) patterns of as-cast HPDC EV42, EVA421A, and EVA421B alloys. Diffraction peaks corresponding to α-Mg, $Mg_{12}RE$, Mg_3RE, Al_2RE_3, and $Al_{11}RE_3$ phases are marked.

$$B_{VRH}=\frac{B_V+B_R}{2} \tag{7}$$

$$E=\frac{9BG}{3B+G} \tag{8}$$

$$v=\frac{3B-E}{6B}=\frac{3B-2G}{2(3B+G)} \tag{9}$$

3. Microstructure of aged die-cast Mg-RE-Al alloy

3.1. XRD results

Fig. 3 illustrates the XRD patterns of as-cast HPDC EV42, EVA421A, and EVA421B alloys with varying Al contents. Firm diffraction peaks corresponding to α-Mg and $Mg_{12}RE$ are observed in all alloys, indicating that these are the dominant phases regardless of the addition of Al. For the EV42 alloy without Al, additional peaks are present that are assigned to the Mg_3RE phase. When 0.5 wt.% Al is added, weak diffraction peaks associated with Al-RE intermetallics emerge, while the Mg_3RE peaks become less pronounced. These observations suggest that a small amount of Al promotes the preferential formation of Al-RE phases over Mg-RE phases. Notably, the weak peaks tentatively indexed as Al_2RE_3 in the 0.5 wt.% Al alloy may partially overlap with reflections of $Al_{11}RE_3$. Therefore, XRD alone cannot completely exclude the presence of a trace amount of $Al_{11}RE_3$ at 0.5 wt.% Al, especially considering the limited volume fraction of Al-RE phases. As the Al content increases to 1.0 wt.%, prominent peaks of the $Al_{11}RE_3$ phase appear, while reflections associated with Al_2RE_3 are no longer discernible. Overall, these results indicate a composition-dependent shift in the dominant GB intermetallics from Mg-RE to Al-RE phases, and from Al_2RE_3-dominant to $Al_{11}RE_3$-dominant with increasing Al content. Note that intermetallic phases with low volume fractions may be difficult to identify by XRD due to detection limits.

3.2. Overall microstructure

Fig. 4 summarizes the OM, SEM, electron backscatter diffraction-inverse pole figure (EBSD-IPF), and grain size statistics for the HPDC EV42, EVA421A, and EVA421B alloys. Fig. 4a, e, and i present polarized optical microscopy observation results, showing color-contrasting grains arising from orientation differences. The results indicate that all alloys exhibit predominantly equiaxed grains, with no significant elongated or oriented grains observed. Furthermore, no obvious macro defects were detected in the examined regions of each alloy, and GBs appear well-defined.

The SEM images in Fig. 4b, f, and j reveal the presence of two distinct grain sizes across all alloys, consistent with grain behavior typical of the HPDC process. Furthermore, all alloys exhibit a network-like skeletal structure with distinct secondary phase formations on this framework. However, network morphology and connectivity vary among alloys due to compositional differences. Specifically, the network in Fig. 4b for the EV42 alloy is fine and continuous, whereas the network in Fig. 4f for the EVA421A alloy exhibits localized refinement and sparse, discrete secondary phase particles, while maintaining its primary network. Conversely, in Fig. 4j, the EVA421B alloy exhibits a bead-chain-like network structure, exhibiting reduced overall connectivity and a marked increase in secondary phase content. Grain size analysis of the alloys was performed using EBSD-IPF maps, as shown in Fig. 4c, g, and k. The histograms of grain size statistics in Fig. 4d, h, and l exhibit the typical bimodal grain size distribution characteristic of HPDC. The measured average grain sizes were 6.5 ± 4.1 μm for EV42 alloy, 6.4 ± 4.2 μm for EVA421A alloy, and 5.2 ± 3.1 μm for EVA421B alloy. It is evident that the average grain size of the EVA421A alloy with 0.5 wt.% Al addition is essentially equivalent to that of EV42 alloy. When Al was increased to 1.0 wt.%, the average grain size of the EVA421B alloy decreased to approximately 5.2 μm. The trend observed in SEM images is consistent with this result, indicating that higher Al levels alter the GB network morphology and increase the density of heterogeneous nucleation sites, leading to significant grain refinement.

Fig. 5 presents a quantitative comparison of the area fractions of intermetallic compounds in GBs across alloys. The major phase transitions from 19.8% in the EV42 alloy to 18.6% in the EVA421A alloy, and 18.2% in the EVA421B alloy. The minor phase increased from 0.3% on the EV42 alloys to 1.9% on the EVA421A alloy and 4.5% on the EVA421B alloy. The major phase consists of Mg-RE phases, while the minor phase comprises a mixture of trace Mg-RE and Al-RE phases. The total area fractions of GB intermetallic compounds were 20.1%, 20.5%, and 22.7%, respectively. Consequently, the addition of 0.5 wt.% Al led to a modest decrease in the major phase fraction, accompanied by a concomitant increase in the minor phase fraction, resulting in a negligible

Please cite this article as: L. Feng, X. Dong, S. Wang et al., Tailoring microstructure and mechanical properties of high-pressure die-cast Mg-RE-Gd alloys via trace Al additions, Journal of Magnesium and Alloys, https://doi.org/10.1016/j.jma.2026.102023

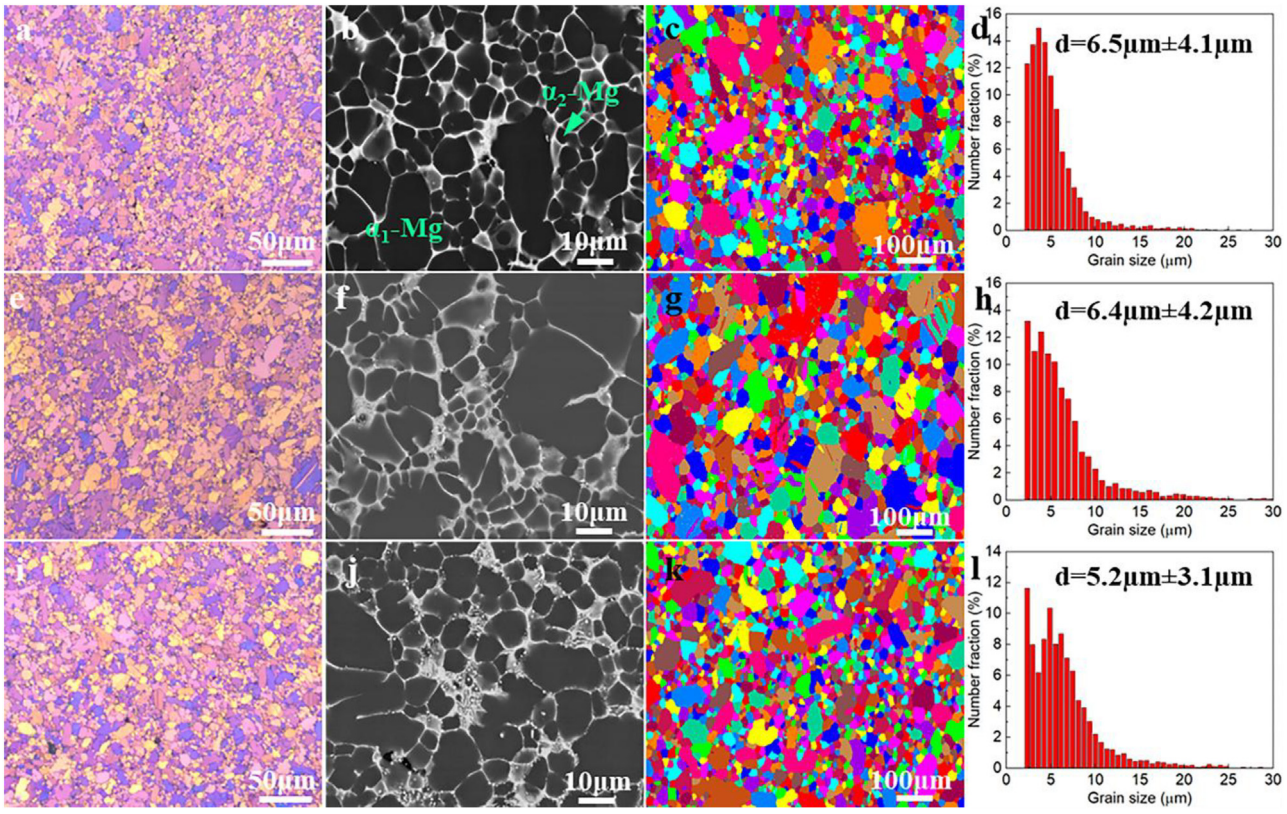

Fig. 4. As-cast microstructures of HPDC EV42, EVA421A, and EVA421B alloys. (a, e, i) Polarized OM images; (b, f, j) SEM images; (c, g, k) EBSD-IPF images; (d, h, l) Grain size histograms. By alloys: (a–d) EV42; (e–h) EVA421A; (i–l) EVA421B. Dual α-Mg grains marked with cyan color.

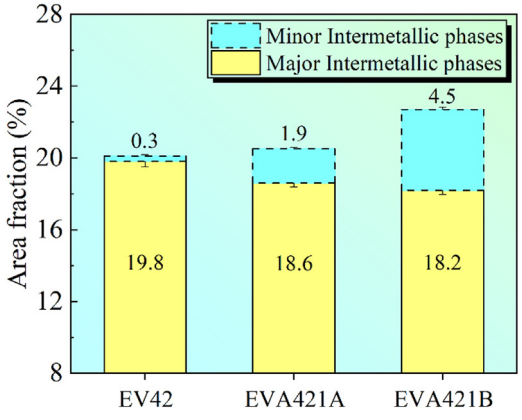

Fig. 5. Quantitative comparison of intermetallic compound area fractions in as-cast HPDC alloys: EV42, EVA421A, and EVA421B. Stacked column charts distinguish major phases in blue from minor phases in yellow.

overall increase. The addition of 1.0 wt.% Al led to a further shift in the composition toward the Al-RE minor phase, thereby achieving the maximum total fraction.

Fig. 6 presents the as-cast BSE-SEM images and corresponding EDS area scanning results for the three alloys, EV42, EVA421A, and EVA421B. The left column displays BSE images, with dashed boxes indicating element mapping regions. The right column presents distribution maps for Mg, La, Ce, Zn, Nd, Gd, Mn, and Al. As illustrated in Fig. 6a for EV42, La, Ce, Nd, and Gd demonstrate distinguishable enrichment along the GB network, while the signals for Zn and Mn appear comparatively negligible. As illustrated in Fig. 6b for EVA421A alloy, REs exhibit a notable enrichment at GBs. Concurrently, Al signals co-localized with Nd and Gd appear at GBs, forming Al-RE enrichment zones. The presence of Zn and Mn at GBs is discernible in this specimen, though with reduced intensity compared to the REs. As illustrated in Fig. 6c, the Al signal at GBs in the EVA421B alloy exhibited a marked intensification and expansion of its coverage. Both strip-like and blocky boundary features exhibited co-enrichment of Al and RE. Zn enrichment along the GB network became more continuous and pronounced near strip-like phases, while Mn was primarily distributed near block-like Al-RE intermetallic compounds. The distinct distribution characteristics may be attributed to the differing crystal compatibility and chemical affinity of the two elements with the Al-RE phase.

3.3. Characterization of intermetallic phases

3.3.1. Overall intermetallic phases

Fig. 7 illustrates the high-magnification BSE-SEM morphology of the GB region in as-cast HPDC EV42, EVA421A, and EVA421B alloys. Fig. 7 presents a representation of the alloys, which is composed of an α-Mg matrix and a continuous network-like $Mg_{12}RE$ phase that is distributed along GBs.

Please cite this article as: L. Feng, X. Dong, S. Wang et al., Tailoring microstructure and mechanical properties of high-pressure die-cast Mg-RE-Gd alloys via trace Al additions, Journal of Magnesium and Alloys, https://doi.org/10.1016/j.jma.2026.102023

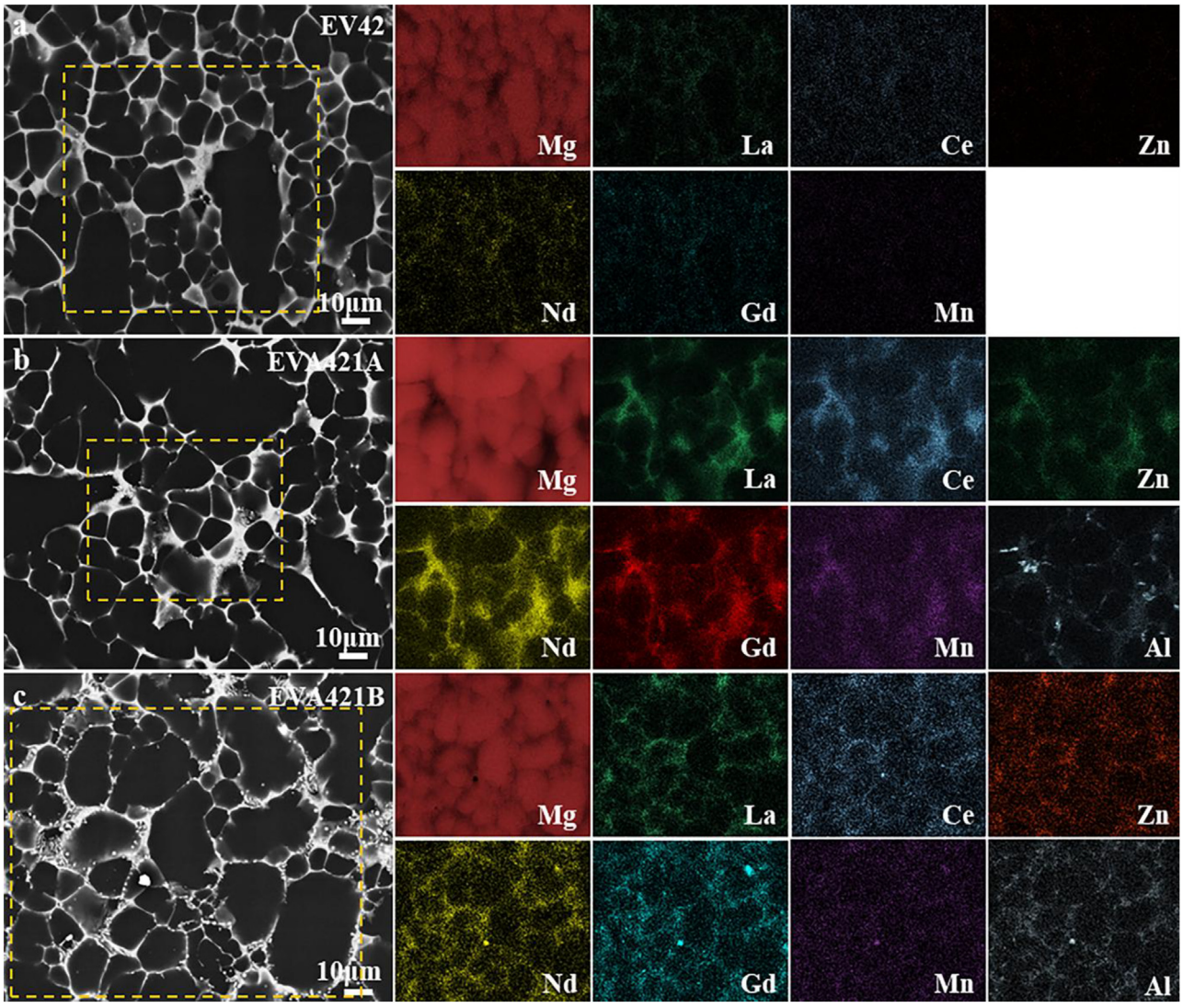

Fig. 6. BSE-SEM mapping of the as-cast HPDC EV42, EVA421A, and EVA421B alloys; (a) EV42, (b) EVA421A, (c) EVA421B.

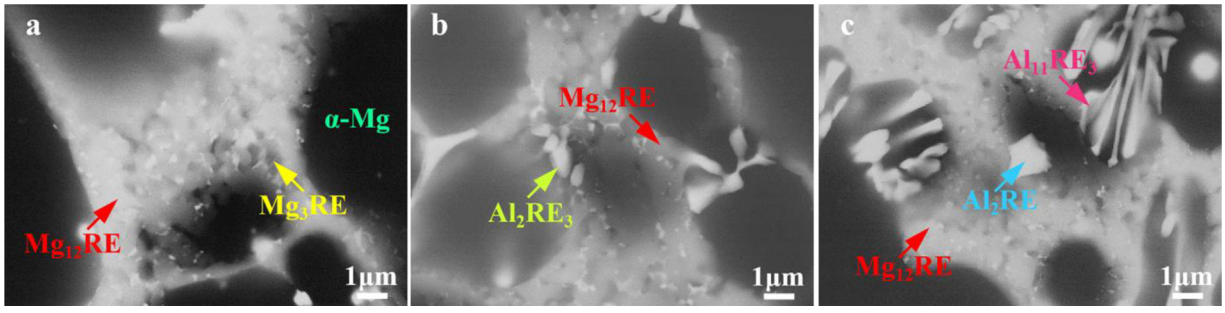

Fig. 7. High-magnification BSE-SEM images of grain-boundary regions in as-cast HPDC alloys. (a) EV42, (b) EVA421A, and (c) EVA421B. A continuous $Mg_{12}RE$ network marked with red arrows. Plate-like Mg_3RE phase in EV42 marked with a yellow arrow. Petal-like Al_2RE_3 phase in EVA421A marked with lime arrow. Strip-like $Al_{11}RE_3$ and block-like Al_2RE phases in EVA421B are marked with magenta and cyan arrows, respectively.

Fig. 7a illustrates that, in the EV42 alloy, the fine, plate-like Mg_3RE phases are localized and form within the network. As illustrated in Fig. 7b, the EVA421A alloy demonstrates a predominant intergranular network $Mg_{12}RE$ phase following the addition of 0.5 wt.% Al, accompanied by the formation of petal-like Al_2RE_3 intergranular precipitates. As illustrated in Fig. 7c, the EVA421B alloy demonstrates that an augmentation in Al content to 1.0 wt.% results in the formation of both strip-like $Al_{11}RE_3$ and block-like Al_2RE intermetallic compounds within the GB. Subsequent TEM results subse-

Please cite this article as: L. Feng, X. Dong, S. Wang et al., Tailoring microstructure and mechanical properties of high-pressure die-cast Mg-RE-Gd alloys via trace Al additions, Journal of Magnesium and Alloys, https://doi.org/10.1016/j.jma.2026.102023

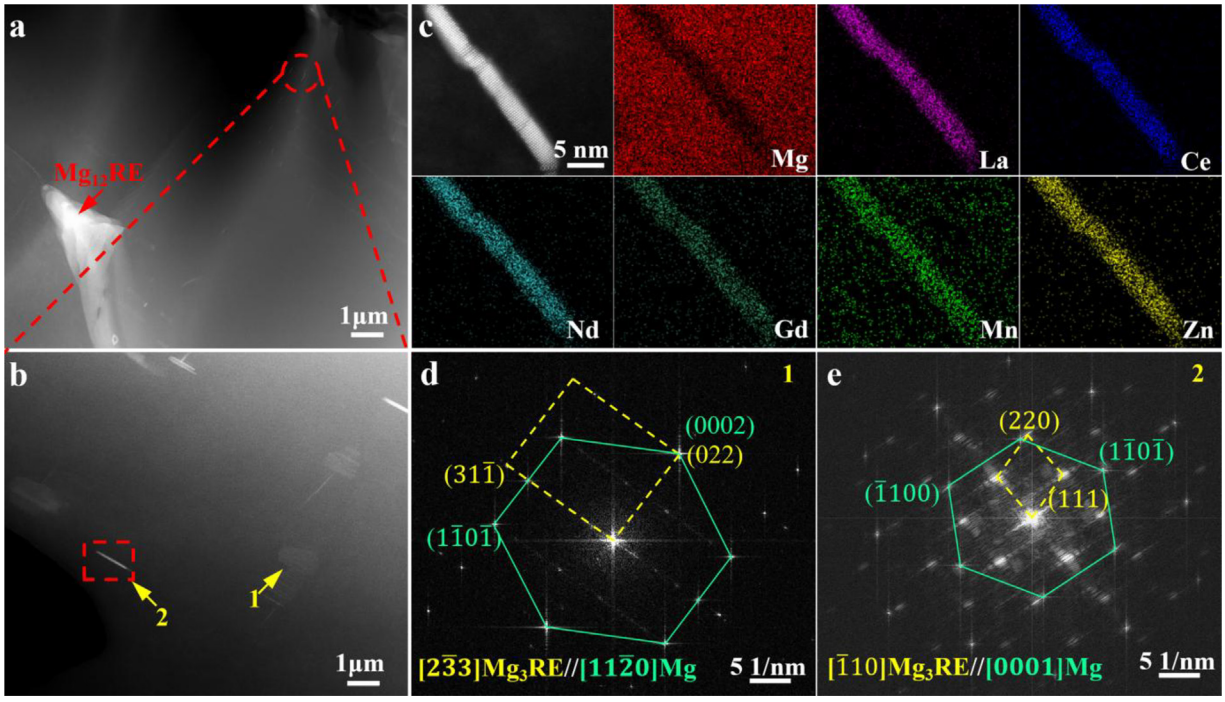

Fig. 8. STEM images for the microstructure of the as-cast HPDC EV42 alloy. (a) STEM-HADDF image of the major intermetallic $Mg_{12}RE$ phase at GB; (b) STEM-HADDF image of the minor intermetallic Mg_3RE phase near the GB; (c) EDX-STEM mapping result of minor intermetallic Mg_3RE phase observed near the GB in b; (d, e) FFT pattern of the minor intermetallic Mg_3RE phases near the GB observed along [2$\bar{3}$3] and [$\bar{1}$10] zone axes, respectively.

quently corroborated the specific phase identification of the aforementioned GB constituents.

3.3.2. Intermetallic phase in 0Al addition

Fig. 8 shows a detailed STEM analysis of intermetallic phases in the Al-free HPDC EV42 alloy. The major intermetallic phase identified at the GB is $Mg_{12}RE$ in Fig. 8a, as demonstrated in the previous study of Gd addition and XRD results in Fig. 3. A plate-like intermetallic phase near the GBs can be observed in Fig. 8a. According to Fig. 8c, the intermetallic phase contains Mg, RE, Zn and Mn, and the analysis of the FFT diffraction pattern in Fig. 8d and e shows that the intermetallic phase is the Mg_3RE phase (face-centered cubic, a = 0.74, Fm-3 m) [42,43]. The Mg_3RE phase is often observed in cast alloys as a sub-stable phase in Mg-RE alloys [44]. Furthermore, the STEM-HAADF image in Fig. 8c shows that the long-plate phase is formed by two small plate-like phases joined by two to three atomic layers in the middle. However, the two plate-like phases do not exhibit a torsional relationship but are directly connected, which differs from the β_1 phase reported for Mg-Gd alloys [43] but is consistent with the β_1 phase observed in studies of Mg-Nd alloys [45]. The information on the intermediate phase, which acts as a linkage, still requires further discussion.

3.3.3. Intermetallic phase in 0.5Al addition

Fig. 9 displays the TEM morphology of the intermetallic phases at GBs of the die-cast EVA421A alloy under as-cast conditions. The continuous network of intermetallic compounds on GBs in Fig. 9a corresponds to the $Mg_{12}RE$ phase, as confirmed by SAED results in Fig. 9b and c and consistent with reports in Mg-La/Ce/Nd alloys [6,46]. The SEM-EDX results in Fig. 6b show that the petal-like intermetallic compound formed on the GBs in the 0.5 wt.% Al-added alloy is the Al-RE phase mainly enriched in Nd and Gd. The SAED results for the intermetallic compound at point A in Fig. 9d–f show that the petal-like intermetallic compound would be the Al_2RE_3 phase (Tetragonal, a = 0.834, c = 0.766, P42nm) [47]. The SEM-EDX results for point A in Table 3 show that the petal-like intermetallic compound has an Al:(Nd, Gd) ratio approximately equal to 0.67, further confirming that the phase is Al_2RE_3. The analysis of the SAED pattern in Fig. 9f shows the Al_2RE_3 phase at zone axes $[110]_{Al2RE3}//[\bar{1}\bar{1}1]_{Mg12RE}$, mainly adjacent to $Mg_{12}RE$. This is consistent with the XRD results in Fig. 3.

3.3.4. Intermetallic phase in 1.0Al addition

Fig. 10 displays the TEM morphology of the intermetallic phases at GBs of the HPDC EVA421B alloy under as-cast conditions. The network intermetallic compound in Fig. 10a tends to be discontinuous compared to the 0.5 wt.% Al added alloy. The SAED result for point 1 in Fig. 10d shows that the network intermetallic compound should be $Mg_{12}RE$. Fig. 10a shows that two other intermetallic compounds are also present at the GBs, a primary strip-like and a secondary blocky phase.

The SAED results for point 2 in Fig. 10g indicate that the blocky intermetallic compound is the Al_2RE phase (cubic, a = 7.899, Fd-3 m) [48]. The SAED results for point C in Fig. 10f confirm that the blocky phase is the Al_2RE phase. The EDX result for point C in Table 3 shows an Al:(Nd,

Please cite this article as: L. Feng, X. Dong, S. Wang et al., Tailoring microstructure and mechanical properties of high-pressure die-cast Mg-RE-Gd alloys via trace Al additions, Journal of Magnesium and Alloys, https://doi.org/10.1016/j.jma.2026.102023

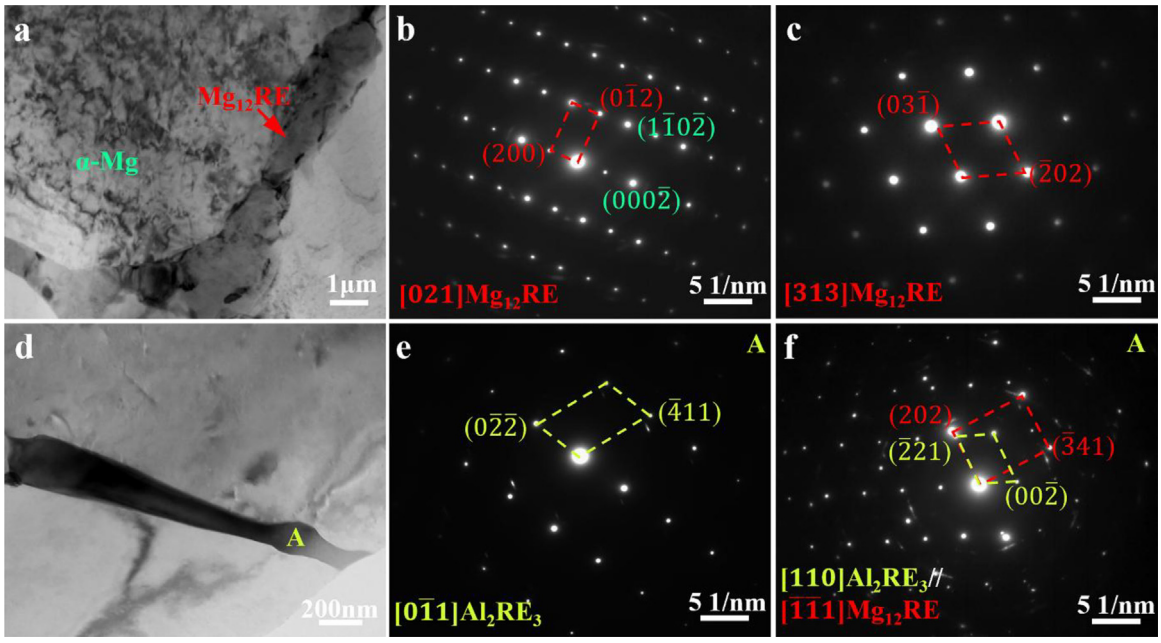

Fig. 9. TEM/STEM images for the microstructure of the as-cast HPDC EVA421A alloy. (a) BF-TEM image of the major intermetallic $Mg_{12}RE$ phase at GB; (b, c) SAED of $Mg_{12}RE$ phase observed along [021] and [313] zone axes; (d) BF-TEM image of the minor intermetallic Al_2RE_3 phase at GBs; (e) SAED of Al_2RE_3 phase observed along [0$\bar{1}$1] zone axes; (f) SAED of Al_2RE_3 phase and $Mg_{12}RE$ phase observed along [110] and [$\bar{1}\bar{1}$1] zone axes, respectively.

Table 3
EDX spot scanning results (at.%) in the as-cast HPDC EVA421A and EVA421B alloy. The selected points are illustrated in Figs. 9 and 10.

Point	Mg	Al	Nd	Gd	La	Ce	Zn	Mn
A	89.1 ± 1.4	4.1 ± 0.5	1.6 ± 0.3	4.5 ± 0.4	0.2 ± 0.1	0.3 ± 0.2	0.2 ± 0.1	0.0 ± 0.0
B	84.3 ± 0.6	12.4 ± 0.8	1.1 ± 0.2	1.2 ± 0.1	1.1 ± 0.2	0.4 ± 0.3	0.1 ± 0.1	0.0 ± 0.0
C	55.9 ± 0.9	26.8 ± 0.6	4.6 ± 0.5	8.1 ± 0.5	1.1 ± 0.4	1.6 ± 0.6	0.6 ± 0.2	1.5 ± 0.6

Gd) ratio of approximately 2.11, further supporting its identification as the Al_2RE phase, consistent with the XRD result. In addition, the morphology of the strip intermetallic compound is shown in Fig. 10b. The SAED results in Fig. 10e for point B indicate that the striped intermetallic compound is the $Al_{11}RE_3$ phase (body-centered orthorhombic, $a = 0.44$, $b = 1.30$, and $c = 1.01$, Immm) [49,50]. The EDX result for point B in Table 3 shows an Al:(Nd, Gd, La, Ce) ratio of approximately 3.27, further confirming that the striped phase is $Al_{11}RE_3$, which is consistent with the XRD results in Fig. 3. The Al_2RE phase was not detected by XRD, probably due to the low volume fraction of the blocky phase, which limits its detectability compared to more abundant phases.

3.4. Mechanical properties

3.4.1. Tensile properties

Fig. 11 illustrates the tensile properties of the HPDC EV42, EVA421A, and EVA421B alloys at RT, 250 °C and 300 °C. Increasing Al content causes the yield strength (YS) to decrease while the elongation (El) and UTS rises at RT. Compared to the EV42 alloy, adding 0.5 wt.% Al and 1.0 wt.% Al reduces YS by approximately 3% and 5.6%, respectively. At 250 °C, these additions decrease YS by 18.5% and 28.5%, while at 300 °C, the reductions are 8.1% and 14.9%. Moreover, the El of alloys containing Al surpasses that of the EV42 alloy and grows with greater Al addition. Detailed average data and standard deviations of the tensile properties for the HPDC EV42, EVA421A, and EVA421B alloys are provided in Supplementary Table S2.

3.4.2. Fracture morphology

Fig. 12 presents the fracture surfaces of HPDC EV42, EVA421A, and EVA421B alloys at RT and high temperatures, thus demonstrating the evolution of fracture behavior induced by Al. As illustrated in Fig. 12a–c, the samples display a mixture of fracture characteristics when examined at RT. The EV42 alloy displays distinctive tear ridges interwoven with toughness dimples, accompanied by intergranular steps. The coexistence of dimples and ridges is indicative of significant localized plastic deformation prior to fracture. In EVA421A, the presence of extensive particle detachment and the formation of dimples along GBs are indicative of void nucleation and localized debonding in proximity to intermetallic compounds. As the Al content increased to 1.0 wt.%, the proportion of stepped fractures rose, indicating enhanced crack penetration through GBs. As illustrated in Fig. 12d–f, at RT, cracks demonstrate an apparent propensity to propagate along GBs and their intermetallic compound networks. In the EV42 alloy, cracks interacting with the $Mg_{12}RE$ frame-

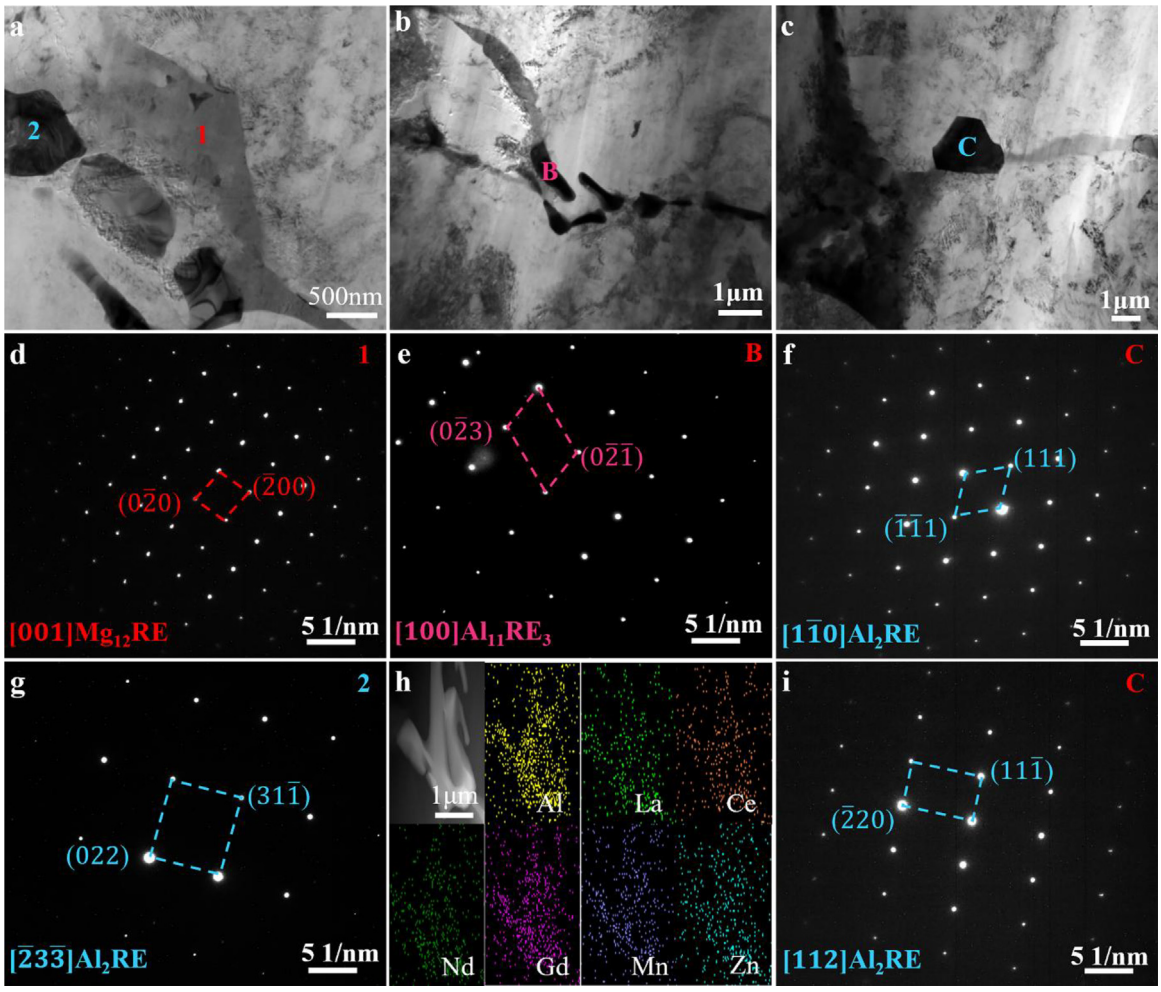

Fig. 10. TEM images for the microstructure of the as-cast HPDC EVA421B alloy. (a) BF image of the major intermetallic $Mg_{12}RE$ phase and block Al_2RE phase at GB; (b) BF image of the $Al_{11}RE_3$ phase at GB; (c) BF image of the block Al_2RE phase on the GBs. (d) SAED of the $Mg_{12}RE$ phase observed along [001] zone axes; (e) SAED of the $Al_{11}RE_3$ phase observed along [100] zone axes; (g) SAED of the Al_2RE phase observed along [$\bar{2}3\bar{3}$] zone axes; (h) EDX mapping result of the $Al_{11}RE_3$ phase on the GBs with Al, La, Ce, Nd, Gd, Mn and Zn elements. (f, i) SAED of Al_2RE phase observed along [1$\bar{1}$0] and [112] zone axes, respectively.

works were arrested by the matrix, indicating enhanced GB pinning and higher local plasticity. In EVA421A, microcracks were initiated in proximity to fine secondary phase particles. In EVA421B, cracks were observed to be coupled around blocky Al_2RE and striped $Al_{11}RE_3$, while a reduced connectivity of the $Mg_{12}RE$ network diminished crack resistance. The results of this study indicate that network connectivity governs damage propagation.

Fig. 12g–i demonstrate that at 250 °C, the fracture mode transitions to intergranular ductile fracture, exhibiting a typical void-ligament morphology. A sponge-like structure composed of circular voids connected by thin ligaments is visible, consistent with a GB-assisted deformation mechanism dominated by GB slip and diffusion-assisted void nucleation, growth, and coalescence. The EV42 displays more discreet voids alongside thicker ligaments, indicating higher intergranular resistance. EVA421A is characterized by the formation of a greater number of voids, while retaining relatively discrete voids with moderately thick ligaments. In EVA421B, voids are larger and more interconnected, while ligaments are thinner and straighter. This phenomenon can be attributed to the bead chaining of the $Mg_{12}RE$ framework and the coarsening of Al-RE particles at GBs, resulting in diminished effective pinning and load transfer efficiency. As demonstrated in Fig. 12j–l, GB-assisted cavitation remains the dominant mechanism at 300 °C. Cavities undergo a process of coarsening and interconnection, while ligaments undergo a process of thinning, thereby reinforcing the characteristics of the void-ligament system. The EV42 exhibited comparatively thick ligaments, with a reduced proportion of flat crystal faces, suggesting an enhanced capacity for damage tolerance. The EVA421A exhibits a higher density of cavities, as well as slightly more slender ligaments. The EVA421B specimen demonstrates the presence of both the largest and most interconnected voids, in conjunction with the thinnest ligaments. Localized flat surfaces, characterized by GB debonding, are also evident. These features are indicative of reduced effective pinning and load transfer, attributable to a weakly intercon-

Please cite this article as: L. Feng, X. Dong, S. Wang et al., Tailoring microstructure and mechanical properties of high-pressure die-cast Mg-RE-Gd alloys via trace Al additions, Journal of Magnesium and Alloys, https://doi.org/10.1016/j.jma.2026.102023

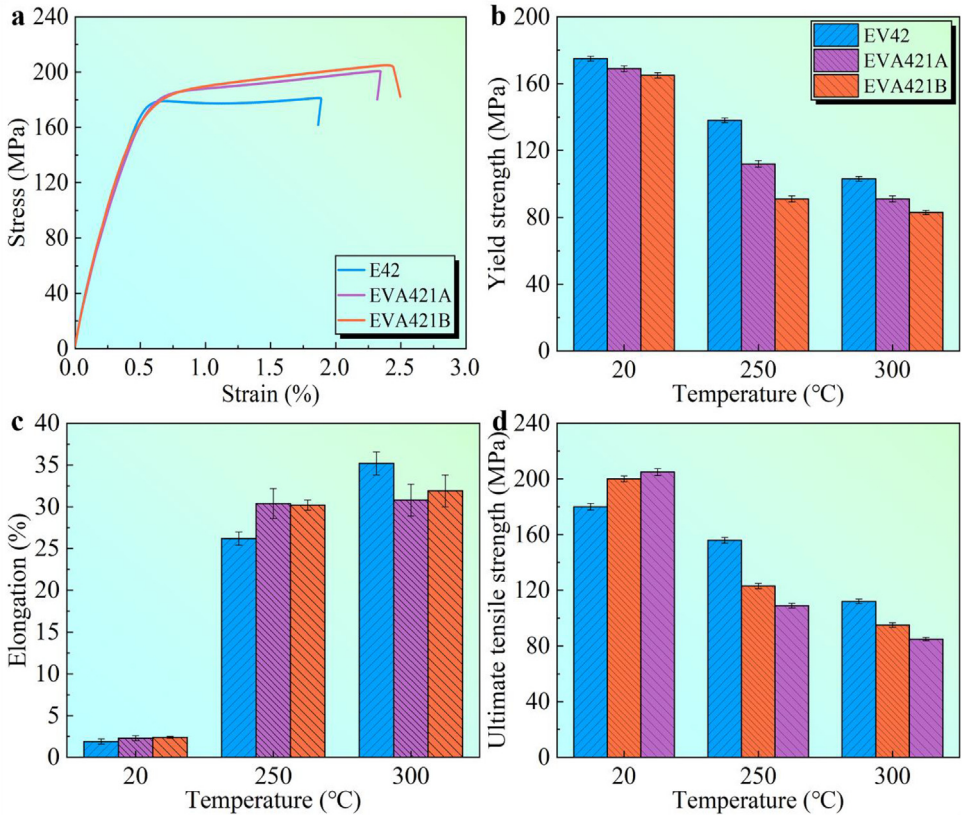

Fig. 11. Mechanical properties of the HPDC EV42, EVA421A, and EVA421B alloys at RT, 250 °C and 300 °C. (a) Stress-strain curve of experimental alloys at RT, (b) comparison of yield strength, (c) comparison of elongation, (d) comparison of ultimate tensile strength. Elongation denotes the total elongation to fracture.

Table 4
The calculated formation enthalpies of single-crystal Mg_3Gd, $Mg_{12}Nd$, Al_2Gd_3, Al_2Gd and $Al_{11}Nd_3$ intermetallic.

Phase	ΔH, eV/atom		
	This work	Reference	
Mg_3Gd	−0.101	−0.140 [51]	−0.087 [52]
$Mg_{12}Nd$	−0.049	−0.042 [53]	−0.047 [54]
Al_2Gd_3	−0.323	−0.345 [55]	-
Al_2Gd	−0.528	−0.541 [55]	−0.520 [56]
$Al_{11}Nd_3$	−0.394	−0.337 [57]	−0.389 [58]

nected $Mg_{12}RE$ framework and coarse Al-RE phases along GBs.

3.5. DFT calculation results

The first-principles calculations at 0 K and 0 GPa were performed for the following representative intermetallics: Mg_3Gd, $Mg_{12}Nd$, Al_2Gd_3, Al_2Gd, and $Al_{11}Nd_3$. The per-atom formation enthalpies ΔH_f are summarized in Table 4 together with literature values for comparison. The present ΔH_f agree well with prior data, supporting the numerical accuracy of our calculations. All ΔH_f are negative, which indicates thermodynamic favorability relative to the constituent elements. The magnitudes follow the sequence:

$$|\Delta H_f|: Mg_{12}Nd < Mg_3Gd < Al_2Gd_3 < Al_{11}Nd_3 < Al_2Gd$$

with Al_2Gd exhibits the most negative ΔH_f among the phases considered, as shown in Fig. 13.

The single-crystal elastic constants C_{ij} are listed in Table 5. All phases satisfy the appropriate Born mechanical stability criteria for their respective crystal systems. Mg_3Gd and Al_2Gd are cubic, $Mg_{12}Nd$ and Al_2Gd_3 are tetragonal, and $Al_{11}Nd_3$ is orthorhombic. Polycrystalline moduli obtained via Voigt-Reuss-Hill averaging are given in Table 6. Fig. 14a and b show that both the bulk modulus B_{VRH} and the shear modulus G_{VRH} increase in the order:

$$Mg_{12}Nd < Mg_3Gd < Al_2Gd_3 < Al_{11}Nd_3 < Al_2Gd$$

Young's modulus E, shown in Fig. 14c, displays the same trend, which indicates that the Al-RE compounds are intrinsically stiffer than the Mg-RE compounds examined.

Ductility tendencies were assessed using the ratio G/B and the Poisson ratio ν as listed in Table 6. With the conventional threshold of 0.57 for the ratio G/B, Fig. 14d demonstrates that $Mg_{12}Nd$, Mg_3Gd, $Al_{11}Nd_3$, and Al_2Gd are classified as brittle because G/B is greater than 0.57, whereas Al_2Gd_3 is classified as ductile because G/B is <0.57. The assessment based on ν is consistent. Fig. 14e shows that values of ν greater than about 0.26 indicate greater ductility, and this condition

Please cite this article as: L. Feng, X. Dong, S. Wang et al., Tailoring microstructure and mechanical properties of high-pressure die-cast Mg-RE-Gd alloys via trace Al additions, Journal of Magnesium and Alloys, https://doi.org/10.1016/j.jma.2026.102023

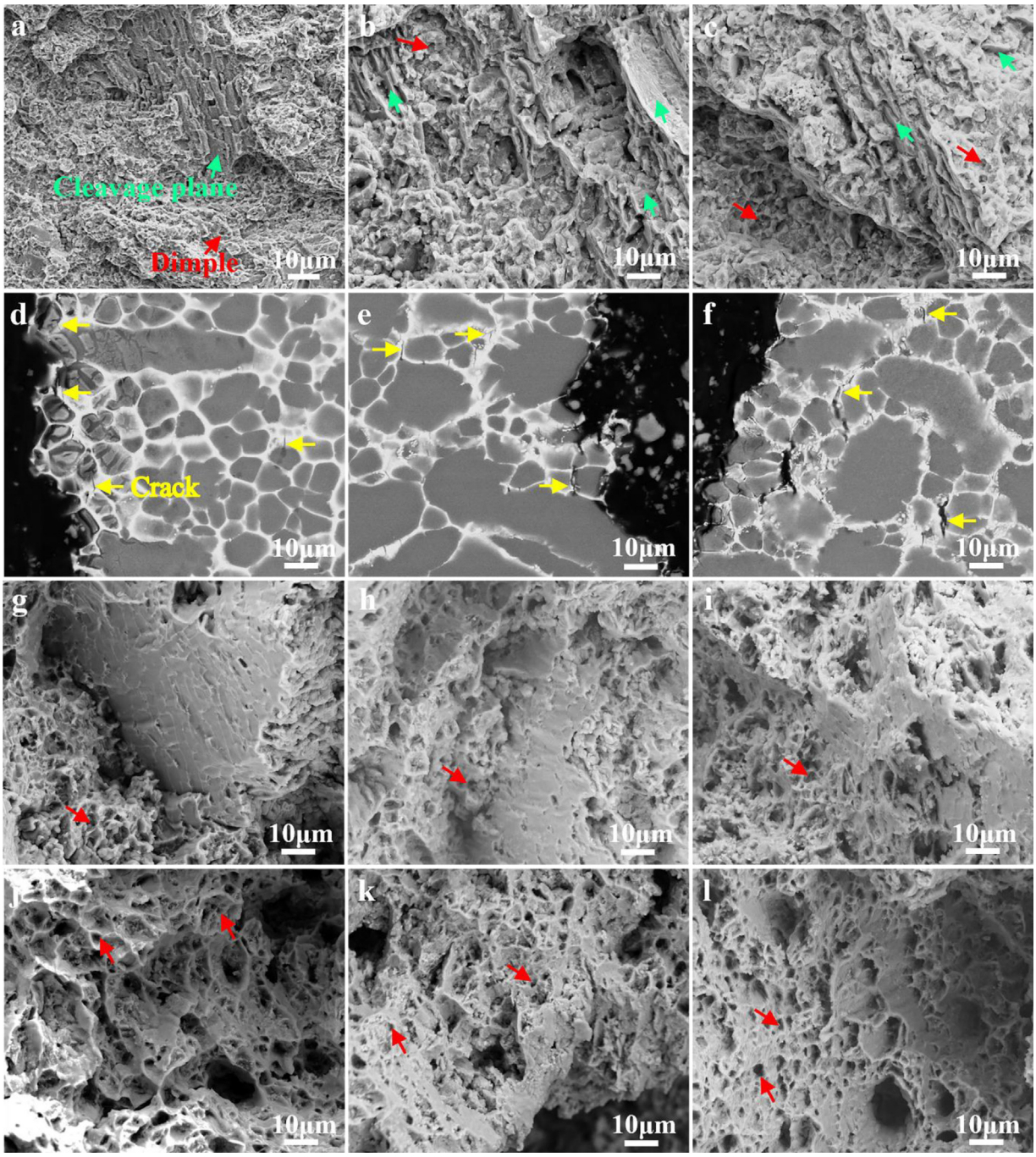

Fig. 12. Fracture surface morphology with BSE-SEM of the HPDC EV42, EVA421A, and EVA421B alloys at RT, 250 °C and 300 °C. (a–c) Micros fracture surface of the cross-section tensile bar at RT, (d–f) Micros fracture surface of the longitudinal-section tensile bar at RT, (g–i) Micros fracture surface of the cross-section tensile bar at 250 °C, (j-l) Micros fracture surface of the cross-section tensile bar at 300 °C, (a, d, g, j) EV42, (b, e, h, k) EVA421A, (c, f, I, l) EVA421B.

Table 5
The calculated elastic constants (C_{ij}) (in GPa) of single-crystal Mg_3Gd, $Mg_{12}Nd$, Al_2Gd_3, Al_2Gd and $Al_{11}Nd_3$ intermetallics.

Phase	C_{ij}								
	C_{11}	C_{22}	C_{33}	C_{44}	C_{55}	C_{66}	C_{12}	C_{13}	C_{23}
Mg_3Gd	58.09	58.09	58.09	40.51	40.51	40.51	31.71	31.71	31.71
$Mg_{12}Nd$	71.41	71.41	57.67	22.65	23.80	23.30	6.71	20.29	20.29
Al_2Gd_3	93.22	93.22	91.41	36.09	36.09	22.60	43.21	36.99	36.99
Al_2Gd	164.68	164.68	164.68	48.42	48.42	48.42	35.02	35.02	35.02
$Al_{11}Nd_3$	123.43	108.78	114.95	61.37	51.00	54.70	48.59	43.84	48.90

Please cite this article as: L. Feng, X. Dong, S. Wang et al., Tailoring microstructure and mechanical properties of high-pressure die-cast Mg-RE-Gd alloys via trace Al additions, Journal of Magnesium and Alloys, https://doi.org/10.1016/j.jma.2026.102023

Table 6
The calculated bulk modulus (B) (in GPa), shear modulus (G) (in GPa), Young's modulus (E) (in GPa), and Poisson's ratio (ν) of polycrystalline Mg_3Gd, $Mg_{12}Nd$, Al_2Gd_3, Al_2Gd, and $Al_{11}Nd_3$ intermetallics.

Phase	B_V	G_V	B_R	G_R	B_{VRH}	G_{VRH}	E	v	G/B	Ductility
Mg_3Gd	40.51	29.58	40.51	22.15	40.51	25.87	63.98	0.24	0.64	Brittle
$Mg_{12}Nd$	32.78	24.17	32.78	23.43	32.78	23.80	57.48	0.21	0.73	Brittle
Al_2Gd_3	56.91	29.67	56.83	28.61	56.87	29.14	74.67	0.28	0.51	Ductile
Al_2Gd	78.24	54.98	78.24	53.88	78.24	54.43	132.55	0.22	0.70	Brittle
$Al_{11}Nd_3$	69.98	47.14	69.90	44.18	69.94	45.66	112.49	0.23	0.65	Brittle

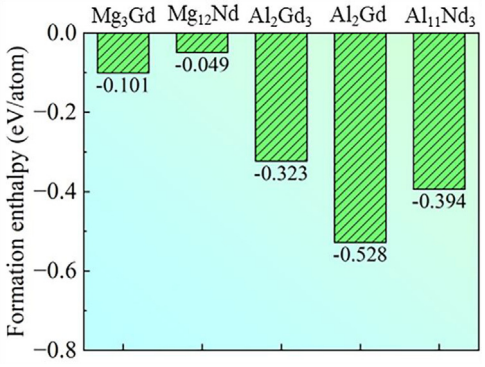

Fig. 13. Theoretical calculation analysis based on DFT for the corresponding formation enthalpy of Mg_3Gd, $Mg_{12}Nd$, Al_2Gd_3, Al_2Gd and $Al_{11}Nd_3$ phases.

is satisfied by Al_2Gd_3, while the remaining phases exhibit smaller values indicative of brittleness. Overall, the Al-RE intermetallic combine higher intrinsic stiffness with, in most cases, limited inherent ductility. This stiffness hierarchy is consistent with the experimentally observed appearance of Al-RE phases at higher Al contents, as shown in Figs. 8–10.

4. Discussion

4.1. Microstructural evolution and strengthening mechanisms

Variations in Al content concurrently impact three strengthening pathways: grain refinement strengthening (σ_{gr}), solution strengthening (σ_{ss}), and second phase strengthening (σ_{sp}) as follows [38,59]:

$$\sigma_{total}=\sigma_0+\sigma_{gr}+\sigma_{ss}+\sigma_{sp} \quad (10)$$

where σ_0 is the intrinsic resistance of the lattice to dislocation motion (21 MPa). Grain refinement was evaluated according to the Hall-Petch relationship [60,61]:

$$\sigma_{gr}=Kd^{-1/2} \quad (11)$$

where d is the grain size, and K is the material constant (0.26 MPa·$m^{1/2}$ for pure Mg) [62,63]. As demonstrated in Fig. 4, the addition of 0.5 wt.% Al does not result in substantial alterations to the grain structure, with EV42 exhibiting an average grain size of 6.5 μm and EVA421A displaying an average grain size of 6.4 μm. However, the addition of 1.0 wt.% Al results in a significant enhancement of grain refinement, leading to an average grain size of 5.2 μm for EVA421B. The presence of Al at a concentration of 0.5% has been observed

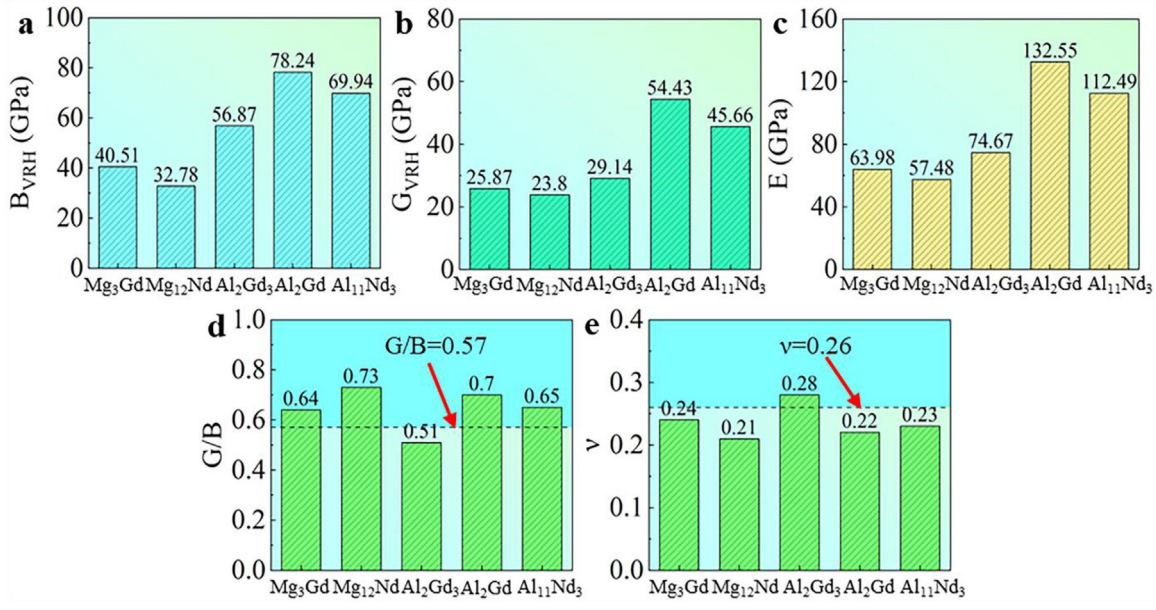

Fig. 14. Intrinsic mechanical strength of Mg_3Gd, $Mg_{12}Nd$, Al_2Gd_3, Al_2Gd and $Al_{11}Nd_3$ phases. (a) Bulk modulus (B_{VRH}). (b) Shear modulus (G_{VRH}). (c) Young's modulus (E). (d) Pugh's ratio (G/B). (e) Poisson's ratio (ν).

to induce the formation of Al-rare earth phases at the GBs. This phenomenon has been shown to result in the local depletion of RE elements, thereby weakening solute drag resistance and concurrently inducing a slight Zeiner pinning effect. It was found that these counteracting effects had negligible effects on grain size. Increasing the Al content to 1.0 wt.% predominantly influenced heterogeneous nucleation capability by Al-RE particles and the Zener pinning effect, consequently leading to substantial grain refinement [64,65]. To assess the grain size strengthening contribution, the Hall-Petch formula, as given in Eq. (11), was employed. The resulting strengthening contributions were 102.1 MPa for EV42 alloy, 102.9 MPa for EVA421A, and 114.2 MPa for EVA421B. Consequently, relative to the Al-free alloy, the strength increased by 0.5 wt.% Al was +0.8 MPa, and the strength increased by 1.0 wt.% Al was +12.1 MPa.

The σ_{ss} was estimated based on the classical theory of Labusch combined with matrix composition analysis via EDX results in Supplementary Fig. S1 and Table S1 [66] in Eq. (12):

$$\sigma_{ss} = \left(\sum_i K_i^{\frac{1}{n}} C_i \right)^n \tag{12}$$

where C_i represents the matrix concentration of solute i, as measured by SEM-EDX and detailed in the Supplementary Table S1. K_i denotes the element-specific factor, and n is a constant set to 2/3 [67]. Comparative analysis in Table S1 suggests that the primary alterations in the matrix composition are attributable to the addition of Al, with concomitant changes in the concentrations of Al, Nd, Gd, and Zn. Although La, Ce, and Mn also exhibit changes, their contributions to σ_{ss} are negligible and thus disregarded. To ensure consistent units, all concentrations in Eq. (12) are expressed as at.%. The factors ki are K_{Al} (196 MPa·(at.)$^{-2/3}$), K_{Zn} (905 MPa·(at.)$^{-2/3}$), K_{Nd} (813 MPa·(at.)$^{-2/3}$), and K_{Gd} (1168 MPa·(at.)$^{-2/3}$), according to the most recent research [68,69]. Utilizing the corrected matrix compositions of the three alloys, the calculated σ_{SS} values for EV42, EVA421A, and EVA421B alloys are 21.3 MPa, 13.5 MPa, and 20.4 MPa, respectively. It is evident that −7.8 MPa considerably diminishes the σ_{SS} for EVA421A in comparison to EV42. It is mainly because Gd and Zn with high solubility are severely depleted from the α-Mg matrix during the formation of Al_2RE_3 intermetallic compounds, while the Al content in solution increases synchronously but contributes little due to its small k_{Al} coefficient. When Al content reaches 1.0, σ_{ss} recovers to a level close to that of 0 Al, approximately −0.9 MPa relative to EV42. It is primarily because the quantity of Al_2Gd phase formed with Gd and Zn participation is minimal, and consequently, it is more efficiently retained within the matrix. Consequently, the dissolved Al content decreases, thereby contributing marginally to the overall effect. Among the three alloys, the relative influence of solute elements in the Labusch equation follows the order Gd $\gtrsim$ Zn $\geq$ Al $\approx$ Nd, which is consistent with their K_i values and measured matrix concentrations.

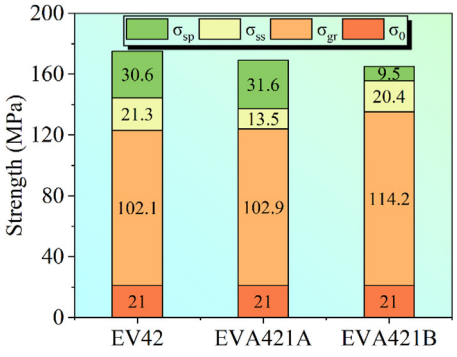

Fig. 15. The contribution of different strengthening mechanisms to the yield strength of HPDC EV42, EVA421A and EVA421B alloys.

The quantitative contribution of σ_{sp} can be determined by employing the residual method in conjunction with computational results from σ_{gr} and σ_{ss}. For EV42, EVA421A, and EVA421B, these values are 30.6, 31.6, and 9.5 MPa, respectively. It is evident that the σ_{sp} of the EVA421B alloy with 1.0 wt.% Al addition is the lowest. A combination of the results from Figs. 4 and 5 reveal a strong correlation with the morphology of intermetallic compounds. In the EVA421A alloy, the continuous network of $Mg_{12}RE$ phase remains dominant, supplemented by a small number of discrete Al-RE particles. This results in a complementary effect between GB dislocation transport and matrix dislocation blocking, making σ_{sp} in the EVA421A alloy equivalent to that of the EV42 alloy. In contrast, the EVA421B alloy with 1.0Al addition exhibits significantly reduced connectivity in the $Mg_{12}RE$ network, with Al-RE particles predominantly forming coarse strip-like and block-like morphologies concentrated near GBs. Although the proportion of discrete Al-RE particles increases gradually with rising Al content and their intrinsic stiffness is higher, their morphological characteristics result in limited pinning of the matrix. This results in a substantial decline in σ_{sp}, thereby diminishing the overall YS of the EVA421B alloy. The detailed contributions of different strengthening mechanisms to the YS of HPDC EV42, EVA421A, and EVA421B alloys are illustrated in Fig. 15.

4.2. Microstructure-property relations at room and elevated temperatures

In the Mg-RE (La/Ce/Nd) system, $Mg_{12}RE$ typically functions as the major intermetallic compound at GBs, often manifesting a continuous network morphology [46,70–72]. In accordance with these findings, $Mg_{12}RE$ was identified as the predominant GB phase in the HPDC alloys examined across varying compositions in Figs. 8–10. As the Al content increases, the morphology and thickness of the $Mg_{12}RE$ network undergo gradual changes, accompanied by the introduction of an Al-RE phase at the GBs. Both extant literature reports and first-principles calculations suggest that the chemical affinity between Al and RE is stronger than between Mg and RE [73]. This phenomenon has been shown to enhance the formation of Al-RE phases as Al activity increases. Con-

Please cite this article as: L. Feng, X. Dong, S. Wang et al., Tailoring microstructure and mechanical properties of high-pressure die-cast Mg-RE-Gd alloys via trace Al additions, Journal of Magnesium and Alloys, https://doi.org/10.1016/j.jma.2026.102023

sequently, the Mg_3RE phases are absent at the GBs of the EVA421A alloy and are replaced by Al_2RE_3 instead. As the Al content increases to 1.0 wt.%, the Al_2RE and $Al_{11}RE_3$ phases partially replace the Al_2RE_3 phase, as illustrated in Figs. 9–10. In contrast to high-Al commercial alloys, such as AE42, AE44 and AEC4112, that readily form dominant striped $Al_{11}RE_3$, within the studied window ($\leq$1.0 wt.% Al), $Mg_{12}RE$ remains the major phase at GBs. This finding highlights the importance of controlled Al content in maintaining the network framework.

It is evident that the YS, when measured at RT, is significantly influenced by the connectivity of the $Mg_{12}RE$ framework. Discretization of the framework has been shown to significantly impact both the values of λ and the efficiency of GB load transfer. This counteracts the beneficial effects of grain refinement and solution strengthening, which are observed at EVA421B alloy. The increase in UTS at RT with Al in Fig. 11d is consistent with Supplementary Fig. S2. Al-containing alloys sustain higher instantaneous work-hardening rates throughout the uniform deformation regime. This produces a larger hardening increment, which delays necking and modestly increases UTS, despite the lower YS.

Deformation at temperatures between 250 °C and 300 °C is primarily driven by GB slip and diffusion-assisted processes. In comparison with discrete Al-RE particles, the continuous $Mg_{12}RE$ network has been shown to pin GBs and increase boundary viscous resistance more effectively, which, in turn, has the effect of suppressing high-temperature softening and creep initiation. Consequently, the root cause of the decrease in high-temperature YS with increasing Al content also lies in the weakening of network connectivity. First-principles results are consistent with the aforementioned microstructure-property relationship. Al-RE compounds are thermodynamically more favorable for formation and exhibit higher intrinsic stiffness than Mg-RE compounds. However, a decline in $Mg_{12}RE$ continuous framework connectivity, along with an increase in the mean free path, significantly reduces the efficiency of translating this stiffness into the load-bearing capacity relationship.

Furthermore, at 300 °C, the potential coarsening of Al-RE phases exacerbates the detrimental effect of the weakened $Mg_{12}RE$ network. The coarse $Al_{11}RE_3$ and Al_2RE particles in the 1.0Al alloy may undergo Ostwald ripening during high-temperature exposure, further compromising interfacial bonding and promoting void nucleation, which collectively lead to the reduced elongation compared to the Al-free alloy.

The characteristics of the newly formed Al-RE phases themselves also directly influence the deformation and damage behavior. As shown in Fig. 5, the area fraction of minor Al-RE dominant phases increases with Al addition. The fine, petal-like Al_2RE_3 particles in the 0.5Al alloy act as effective obstacles to dislocation glide. Their submicron scale and dispersion promote a relatively uniform strain distribution and require dislocations to navigate around them, thereby enhancing the work-hardening rate and contributing to the improved uniform elongation observed in this alloy. In contrast, the coarse, strip-like $Al_{11}RE_3$ and blocky Al_2RE phases in the 1.0Al alloy present larger, incoherent interfaces with the matrix. These interfaces are prone to stress concentration, leading to premature decohesion and void nucleation, as evidenced by the particle-associated dimples and intergranular steps on the fracture surface. This direct damage initiation counteracts their potential strengthening contribution, resulting in the lowest σ_{sp} as quantified in Section 4.1. Therefore, while the connectivity of the $Mg_{12}RE$ network governs the overall load transfer capacity, the size, morphology, and interfacial coherence of the Al-RE phases critically influence the local strain accommodation and damage initiation mechanisms, collectively determining the final strength-ductility balance.

4.3. First-principles implications for microstructure evolution

The DFT calculations in this work were employed to elucidate the fundamental thermodynamic tendency and intrinsic elastic property trends underlying the Al-induced phase evolution. The selected model phases represent the key categories of intermetallics identified experimentally, enabling a comparative assessment of the intrinsic effect of Al addition. The agreement with prior data shown in Table 4 lends confidence to the present computational setup. The calculations reveal a consistent trend that Al-RE compounds exhibit more negative formation enthalpies and higher intrinsic stiffness than their Mg-RE counterparts. This provides a thermodynamic rationale for the preferential formation of Al-RE phases relative to metastable Mg_3RE upon Al addition, as observed experimentally, and suggests a higher local stiffness/constraint potential associated with Al-RE-containing GB regions. It is important to note that while DFT captures this intrinsic tendency, the final microstructure formed under HPDC reflects the interplay between this driving force and the kinetic constraints imposed by rapid solidification.

Specifically, the extremely high cooling rates and applied pressure inherent to the HPDC process constitute a strongly non-equilibrium solidification condition. This leads to limit long-range diffusion, allowing the thermodynamically metastable Mg_3RE phase to be retained in the 0Al alloy and favor kinetically accessible anisotropic morphologies of Al–RE intermetallics, such as the strip-like $Al_{11}RE_3$ in the 1.0Al alloy. Consequently, the observed evolution of Al-RE phase morphology and the changes in $Mg_{12}RE$ network connectivity are essentially the concrete manifestation of the thermodynamic driving force introduced by Al under the specific kinetic pathway constraints of HPDC. DFT calculations clarify the propensity for phase selection, while the processing conditions dictate its ultimate realization form.

However, the macroscopic strengthening outcome is not dictated solely by the intrinsic modulus of individual phases. Instead, it critically depends on the ability of these high-modulus phases to organize into an effective, continuous load-bearing network. As evidenced in Figs. 8–10, the addition of Al, while introducing stiffer Al-RE compounds, concurrently leads to the thinning and eventual fragmentation of the primary $Mg_{12}RE$ network. A continuous $Mg_{12}RE$ framework

Please cite this article as: L. Feng, X. Dong, S. Wang et al., Tailoring microstructure and mechanical properties of high-pressure die-cast Mg-RE-Gd alloys via trace Al additions, Journal of Magnesium and Alloys, https://doi.org/10.1016/j.jma.2026.102023

acts as a percolating skeleton along GBs, providing sustained constraint against intergranular deformation and an efficient pathway for load transfer. In contrast, discrete Al-RE precipitates, despite their higher intrinsic stiffness, primarily offer localized pinning points. Once the continuous framework is disrupted, they cannot establish an equivalent long-range load-bearing pathway. Furthermore, coarser Al-RE phases at GBs may intensify local stress incompatibility and facilitate void nucleation at elevated temperatures, thereby reducing their effective strengthening contribution.

Therefore, the DFT results, combined with microstructural analysis, underscore a crucial principle. The evolution of strength in this alloy system is governed by an interplay between intrinsic phase properties and their spatial network topology. The superior GB pinning and load transfer capabilities afforded by the continuous $Mg_{12}RE$ framework outweigh the benefit of introducing discrete Al-RE phases when the framework connectivity is compromised. This explains the decrease in σ_{sp} contribution in Section 4.1 and the concomitant weakening of strength at both room and elevated temperatures with increasing Al content in Section 4.2.

4.4. Role of Al in alloy design and optimization

The present study demonstrates that a range of 0.5–1.0 wt.% Al achieves a robust balance between grain refinement, phase selection, and thermal stability. Al promotes the preferential growth of thermodynamically stable Al-RE intermetallic compounds at GBs within this range, acting as potential heterogeneous nucleation sites to achieve grain refinement. Simultaneously, due to controlled overall volume fraction, significant phase coarsening and GB embrittlement are avoided, leading to improved high-temperature El. It is crucial to emphasize that the variation in strength does not simply depend on the presence or absence of Al-RE but is more strongly governed by the connectivity of the $Mg_{12}RE$ continuous framework. In the present alloy system under HPDC conditions, when the Al content was increased to 1.0 wt.%, it induced reduced connectivity of the $Mg_{12}RE$ network and coarsening of Al-RE phases, resulting in a decrease in the macroscopic YS due to GB softening and disruption of load transfer pathways. This phenomenon has been noted even in cases where Al-RE possesses high intrinsic stiffness. Al can be regarded as a phase selection lever from an alloy design perspective. Its function is not to unidirectionally increase the second-phase content; instead, it moderates Al-RE while maintaining $Mg_{12}RE$ network connectivity. This balanced regulation can enhance intergranular constraint and load-transfer efficiency at GB regions, and when optimized at trace levels can be beneficial for high-temperature stability.

From an engineering perspective, comparing the EVA421A alloy with the commercia HPDC AE44 alloy holds significant reference value. Table 7 compares the high-temperature tensile properties of a representative EVA421A alloy with those of the commercially available AE44 alloy as reported in the literature [40]. Compared with the commercial AE44 alloy, the EVA421A alloy exhibits substantially higher YS and UTS at 300 °C, while maintaining comparable El within experimental scatter. This advantage stems from the aforementioned aluminum-assisted phase selection mechanism and optimized intergranular intermetallic compound topology. These results highlight the application potential of the alloy in high-temperature. In addition to the short-term tensile benchmarking, the long-term high-temperature stability of the optimized 0.5 wt.% Al alloy has been independently validated in our recent study [41], where a markedly improved creep resistance was reported and attributed to the stabilized intergranular intermetallic topology. These findings support the present phase-selection design concept from a service-reliability perspective, while the long-term exposure behavior of the 1.0 wt.% Al alloy remains to be systematically assessed.

Table 7
Benchmarking of the high-temperature tensile properties of the present EVA421A alloy against the commercial AE44 alloy [40].

Alloy	T (°C)	YS (MPa)	UTS (MPa)	El (%)
EVA421A	300	91 ± 1.8	95 ± 1.7	30.8 ± 1.9
AE44 [40]	300	83 ± 1.3	85 ± 1.2	31.9 ± 1.9

5. Conclusions

The microstructure and tensile properties of the HPDC EV42, EVA421A, and EVA421B alloys at RT and high temperature were studied, and conclusions are summarized below:

1) Trace Al promotes a phase evolution from metastable Mg_3RE in the Al-free alloy to petal-like Al_2RE_3 at 0.5 wt.% Al, and to a coexistence of blocky Al_2RE and strip-like $Al_{11}RE_3$ at 1.0 wt.% Al. $Mg_{12}RE$ remains the dominant GB phase, while its network connectivity decreases.
2) At RT, in HPDC EV42, EVA421A and EVA421B alloys, YS changes from 175 to 169 and 165 MPa, UTS from 180 to 200 and 205 MPa, and El from 1.9% to 2.3% and 2.4%. At 250 °C, El increases and both YS and UTS decrease. At 300 °C, Al-containing alloys maintain high El but remain below that of the Al-free alloy, and YS and UTS decrease with Al addition.
3) At RT, the fracture is mixed quasi-cleavage with dimples. At 250 °C, it transforms to intergranular ductile fracture with a typical void–ligament morphology, and at 300 °C cavities become coarser and more connected while ligaments thin. Reduced $Mg_{12}RE$ connectivity promotes crack penetration and void coalescence.
4) DFT indicates that Al-RE compounds have more negative formation enthalpies and higher elastic moduli. Moreover, a continuous $Mg_{12}RE$ framework provides better GB pinning and load transfer.
5) An Al level near 0.5 wt.% tends to better preserve the $Mg_{12}RE$ network than 1.0 wt.% Al, offering a more balanced combination of RT strength and elevated-temperature strength and ductility.

Please cite this article as: L. Feng, X. Dong, S. Wang et al., Tailoring microstructure and mechanical properties of high-pressure die-cast Mg-RE-Gd alloys via trace Al additions, Journal of Magnesium and Alloys, https://doi.org/10.1016/j.jma.2026.102023

Declaration of competing interest

The authors declare that they have no known competing financial interests or personal relationships that could have appeared to influence the work reported in this paper.

CRediT authorship contribution statement

Lingyun Feng: Writing – original draft, Methodology, Investigation, Formal analysis. **Xixi Dong:** Writing – review & editing, Supervision, Conceptualization. **Shihao Wang:** Investigation. **Qing Cai:** Investigation. **Hangbiao Mi:** Data curation. **Wei Guo:** Writing – review & editing, Supervision. **Shouxun Ji:** Writing – review & editing, Supervision, Resources.

Acknowledgement

This work has been supported by the National Key Research and Development Program of China (No. 2023YFB4606000), National Outstanding Youth Science Fund Project of National Natural Science Foundation of China, National Natural Science Foundation of China (No. 52575400), Jiangsu Specially-Appointed Professor project and Innovate UK (No. 10113213 and No 103962). The SuperSTEM Laboratory is the UK National Research Facility for Advanced Electron Microscopy, supported by EPSRC under grant number EP/W021080/1. The computation is completed in the HPC Platform of Huazhong University of Science and Technology.

Supplementary materials

Supplementary material associated with this article can be found, in the online version, at doi:10.1016/j.jma.2026.102023.

References

[1] A.A. Luo, Int. Mater. Rev. 49 (2013) 13–30, doi:10.1179/095066004225010497.
[2] Y. Yuan, X. Chen, X. Xiong, K. Li, J. Tan, Y. Yang, X. Peng, X. Chen, D. Chen, F. Pan, J. Magnes. Alloy. 13 (2025) 4689–4732, doi:10.1016/j.jma.2025.09.034.
[3] A.A. Luo, B.R. Powell, M.P. Balogh, Metall. Mater. Trans. A 33 (2002) 567–574, doi:10.1007/s11661-002-0118-1.
[4] K.R. Athul, U.T.S. Pillai, A. Srinivasan, B.C. Pai, Adv. Eng. Mater. 18 (2015) 770–794, doi:10.1002/adem.201500393.
[5] Z. Cui, Y. Liu, Y. Zeng, M. Liu, X. Liu, S. Xu, X. Chen, Q. Wang, J. Magnes. Alloy. 13 (2025) 414–428, doi:10.1016/j.jma.2024.03.015.
[6] X. Wan, M. Yin, C. Zeng, W. Liu, P. Peng, L. Zhang, B. Jia, J. Zhang, Q. Yang, Q. Dai, J. Magnes. Alloy. 13 (2025) 3466–3486, doi:10.1016/j.jma.2025.04.027.
[7] W. Can, H. Peide, Z. Lu, Z. Caili, X. Bingshe, Rare Met. Mater. Eng. 40 (2011) 590–594, doi:10.1016/S1875-5372(11)60030-1.
[8] M. Bamberger, G. Atiya, S. Khawaled, A. Katsman, Metall. Mater. Trans. A 45 (2013) 3241–3253, doi:10.1007/s11661-013-2069-0.
[9] Z. Yu, Y. Huang, L. Liu, K. Shi, B. Du, K. Liu, S. Li, W. Du, Scr. Mater. 220 (2022) 114901, doi:10.1016/j.scriptamat.2022.114901.
[10] S. Gavras, S.M. Zhu, J.F. Nie, M.A. Gibson, M.A. Easton, Mater. Sci. Eng. A 675 (2016) 65–75, doi:10.1016/j.msea.2016.08.046.
[11] F. Qi, X. Zhang, G. Wu, W. Liu, X. He, W. Ding, Mater. Sci. Eng. A 813 (2021) 141172, doi:10.1016/j.msea.2021.141172.
[12] X. Li, H. Shi, X. Li, W. Gan, C. Xu, C. Ding, S. Tursunbaev, N. Turakhodjaev, X. Hu, X. Wang, J. Magnes. Alloy. (2025) 101812, doi:10.1016/j.jma.2025.06.029.
[13] J.L. Li, D. Wu, R.S. Chen, E.H. Han, Acta Mater 159 (2018) 31–45, doi:10.1016/j.actamat.2018.08.013.
[14] T.L. Chia, M.A. Easton, S.M. Zhu, M.A. Gibson, N. Birbilis, J.F. Nie, Intermetallics 17 (2009) 481–490, doi:10.1016/j.intermet.2008.12.009.
[15] S. Golmakaniyoon, R. Mahmudi, Mater. Sci. Eng. A 620 (2015) 301–308, doi:10.1016/j.msea.2014.09.113.
[16] S. Golmakaniyoon, R. Mahmudi, Mater. Sci. Eng. A 528 (2011) 5228–5233, doi:10.1016/j.msea.2011.03.083.
[17] G. Wu, C. Wang, M. Sun, W. Ding, J. Magnes. Alloy. 9 (2021) 1–20, doi:10.1016/j.jma.2020.06.021.
[18] T. Li, J. Song, A. Zhang, G. You, Y. Yang, B. Jiang, X. Qin, C. Xu, F. Pan, J. Magnes. Alloy. 11 (2023) 4166–4180, doi:10.1016/j.jma.2023.11.003.
[19] M.M. Hoseini-Athar, R. Mahmudi, R.P. Babu, P. Hedström, J. Alloy. Compd. 831 (2020) 154766, doi:10.1016/j.jallcom.2020.154766.
[20] S. Liu, Z. Wei, Z. Liu, P. Mao, F. Wang, Z. Wang, L. Zhou, X. Yin, J. Alloy. Compd. 904 (2022) 163963, doi:10.1016/j.jallcom.2022.163963.
[21] D. Gu, J. Peng, J. Wang, F. Pan, Met. Mater. Int. 27 (2020) 1483–1492, doi:10.1007/s12540-019-00588-6.
[22] L. Guan, Y. Deng, A. Luo, X. Guo, C. Tang, Mater. Sci. Eng. A 804 (2021) 140736, doi:10.1016/j.msea.2021.140736.
[23] Q. Zhang, Q. Li, X. Chen, J. Bao, Z. Chen, Mater. Sci. Eng. A 826 (2021) 142026, doi:10.1016/j.msea.2021.142026.
[24] J. She, J. Chen, X. Xiong, Y. Yang, X. Peng, D. Chen, F. Pan, J. Magnes. Alloy. 12 (2024) 3441–3475, doi:10.1016/j.jma.2024.10.001.
[25] T. Honma, T. Ohkubo, S. Kamado, K. Hono, Acta Mater. 55 (2007) 4137–4150, doi:10.1016/j.actamat.2007.02.036.
[26] D. Xu, E.-H. Han, Y. Xu, Prog. Nat. Sci. Mater. Int. 26 (2016) 117–128, doi:10.1016/j.pnsc.2016.03.006.
[27] H. Liu, H. Huang, C. Wang, J. Sun, J. Bai, F. Xue, A. Ma, X.-B. Chen, JOM 71 (2019) 3314–3327, doi:10.1007/s11837-019-03610-9.
[28] M.S. Geshani, P.M. Kalayeh, A.H. Asadi, H. Mirzadeh, M. Malekan, M. Emamy, J. Mater. Res. Technol. 24 (2023) 4945–4966, doi:10.1016/j.jmrt.2023.04.105.
[29] L. Feng, X. Dong, M. Xia, X. Zhu, G. Ji, H. Yang, B. Wang, E.A. Nyberg, S. Ji, J. Mater. Res. Technol. 22 (2023) 2955–2966, doi:10.1016/j.jmrt.2022.12.125.
[30] X. Dong, L. Feng, S. Wang, F. Wang, R. Ghasemi, G. Ji, E.A. Nyberg, S. Ji, Materialia 22 (2022) 101426, doi:10.1016/j.mtla.2022.101426.
[31] Q. Yang, X. Wu, X. Qiu, Materials (Basel) 16 (2023) 1954, doi:10.3390/ma16051954.
[32] Y. Ma, S.-Y. Yu, Y.M. Kim, T. Lee, B.-C. Suh, J. Magnes. Alloy. 13 (2025) 3066–3080, doi:10.1016/j.jma.2025.06.006.
[33] N. Mo, Q. Tan, M. Bermingham, Y. Huang, H. Dieringa, N. Hort, M.-X. Zhang, Mater. Des. 155 (2018) 422–442, doi:10.1016/j.matdes.2018.06.032.
[34] H. Cai, N. Zhang, L. Liu, J. Su, Y. Li, Y. Kang, F. Guo, J. Magnes. Alloy. 12 (2024) 3094–3114, doi:10.1016/j.jma.2024.06.021.
[35] R.V. Marode, T.A. Lemma, N. Sallih, S.R. Pedapati, M. Awang, A. Hassan, J. Magnes. Alloy. 12 (2024) 2091–2146, doi:10.1016/j.jma.2024.06.007.
[36] M.S. Dargusch, K. Pettersen, P. Bakke, K. Nogita, A.L. Bowles, G.L. Dunlop, Int. J. Cast Met. Res. 17 (2013) 170–173, doi:10.1179/136404604225017555.
[37] W. Xiao, M.A. Easton, S. Zhu, M.S. Dargusch, M.A. Gibson, S. Jia, J. Nie, Adv. Eng. Mater. 14 (2011) 68–76, doi:10.1002/adem.201100149.
[38] J. Rong, W. Xiao, X. Zhao, Y. Fu, H. Liao, C. Ma, M. Chen, C. Huang, J. Alloy. Compd. 896 (2022) 162943, doi:10.1016/j.jallcom.2021.162943.
[39] X. Zhao, Z. Li, W. Zhou, D. Li, M. Qin, X. Zeng, J. Mater. Res. 36 (2021) 3145–3154, doi:10.1557/s43578-021-00319-x.

[40] X. Dong, L. Feng, S. Wang, E.A. Nyberg, S. Ji, J. Magnes. Alloy. 9 (2021) 90–101, doi:10.1016/j.jma.2020.09.012.
[41] X. Dong, L. Feng, S. Wang, G. Ji, A. Addad, H. Yang, E.A. Nyberg, S. Ji, Acta Mater 232 (2022) 117957, doi:10.1016/j.actamat.2022.117957.
[42] J. Zuo, M. Zhang, T. Nakata, G. Wang, D. Li, H. Shi, C. Xu, X. Wang, W. Li, G. Fan, L. Geng, S. Kamado, Materials (Basel) 15 (2022) 1632, doi:10.3390/ma15051632.
[43] X. Gao, S.M. He, X.Q. Zeng, L.M. Peng, W.J. Ding, J.F. Nie, Mater. Sci. Eng. A 431 (2006) 322–327, doi:10.1016/j.msea.2006.06.018.
[44] D. Wang, M. Amsler, V.I. Hegde, J.E. Saal, A. Issa, B.-C. Zhou, X. Zeng, C. Wolverton, Acta Mater. 158 (2018) 65–78, doi:10.1016/j.actamat.2018.07.041.
[45] Y.M. Zhu, H. Liu, Z. Xu, Y. Wang, J.F. Nie, Acta Mater 83 (2015) 239–247, doi:10.1016/j.actamat.2014.09.037.
[46] M.-X. Zeng, R.-N. Wang, B.-Y. Tang, L.-M. Peng, W.-J. Ding, Modell. Simul. Mater. Sci. Eng. 20 (2012) 035018, doi:10.1088/0965-0393/20/3/035018.
[47] N.C. Baenziger, J.J. Hegenbarth, Acta Cryst 17 (1964) 620–621, doi:10.1107/S0365110X64001499.
[48] A. Śalebarski, Phys. Status Solidi A 46 (1978) K29–K34, doi:10.1002/pssa.2210460161.
[49] Q. Yang, T. Zheng, D. Zhang, X. Liu, J. Fan, X. Qiu, X. Niu, J. Meng, J. Alloy. Compd. 572 (2013) 129–136, doi:10.1016/j.jallcom.2013.03.196.
[50] A.H. Gomes de Mesquita, K.H.J. Buschow, Acta Cryst 22 (1967) 497–501, doi:10.1107/S0365110X67001045.
[51] L. Lin, P. Liang, L. Yang, L.J. Chen, Z. Liu, Y.M. Wang, Mater. Sci. Eng. A 527 (2010) 2643–2648, doi:10.1016/j.msea.2010.01.027.
[52] X.Y. Meng, X.H. Wen, Y.P. Ren, G.W. Qin, Mater. Sci. Technol. 28 (2012) 794–798, doi:10.1179/1743284711Y.0000000086.
[53] X. Tao, Y. Ouyang, H. Liu, Y. Feng, Y. Du, Y. He, Z. Jin, J. Alloy. Compd. 509 (2011) 6899–6907, doi:10.1016/j.jallcom.2011.03.177.
[54] C. Zhai, Q. Luo, Q. Cai, R. Guan, Q. Li, J. Alloy. Compd. 773 (2019) 202–209, doi:10.1016/j.jallcom.2018.09.203.
[55] C. Colinet, A. Pasturel, K.H.J. Buschow, Phys. B Condens. Matter. 150 (1988) 397–403, doi:10.1016/0378-4363(88)90080-0.
[56] H.L. Chen, L. Lin, P.L. Mao, Z. Liu, J. Magnes. Alloy. 3 (2015) 197–202, doi:10.1016/j.jma.2015.08.003.
[57] H. Yamamoto, M. Morishita, M. Kusumoto, J. Alloy. Compd. 433 (2007) 1–5, doi:10.1016/j.jallcom.2006.06.030.
[58] X.-Q. Wang, R.-X. Song, D. Wang, X. Guan, S. Li, S. Sun, H. Yang, X. Wang, D. Wu, G. Tu, S. Li, H.-L. Yan, L. Zuo, J. Mater. Sci. Technol. 214 (2025) 278–291, doi:10.1016/j.jmst.2024.06.044.
[59] Y. Xu, F. Gensch, Z. Ren, K.U. Kainer, N. Hort, Prog. Nat. Sci. Mater. Int. 28 (2018) 724–730, doi:10.1016/j.pnsc.2018.10.002.
[60] R. Zhao, W. Zhu, J. Zhang, L. Zhang, J. Zhang, C. Xu, Mater. Sci. Eng. A 788 (2020) 139594, doi:10.1016/j.msea.2020.139594.
[61] X. Dong, Y. Zhang, S. Ji, Mater. Sci. Eng. A 700 (2017) 291–300, doi:10.1016/j.msea.2017.06.005.
[62] C.H. Caceres, G.E. Mann, J.R. Griffiths, Metall. Mater. Trans. A 42 (2011) 1950–1959, doi:10.1007/s11661-010-0599-2.
[63] G.W. An, S.-C. Jin, T. Lee, S. Jo, S.H. Park, J. Magnes. Alloy. 13 (2025) 3004–3019, doi:10.1016/j.jma.2025.04.020.
[64] M. Wu, J. Chen, H. Yan, W. Xia, B. Su, Y. Deng, Y. Shen, Mater. Sci. Eng. A 861 (2022) 144322, doi:10.1016/j.msea.2022.144322.
[65] S.M. Zhu, M.A. Gibson, J.F. Nie, M.A. Easton, T.B. Abbott, Scr. Mater. 58 (2008) 477–480, doi:10.1016/j.scriptamat.2007.10.041.
[66] H. Cai, F. Guo, J. Su, L. Liu, Mater. Res. Express. 6 (2019) 066541, doi:10.1088/2053-1591/ab090b.
[67] W. Sun, B. Wu, H. Fu, X.-S. Yang, X. Qiao, M. Zheng, Y. He, J. Lu, S.-Q. Shi, J. Mater. Sci. Technol. 99 (2022) 223–238, doi:10.1016/j.jmst.2021.04.074.
[68] L. Gao, R.S. Chen, E.H. Han, J. Alloy. Compd. 481 (2009) 379–384, doi:10.1016/j.jallcom.2009.02.131.
[69] Y. Li, S. Yin, G. Zhang, X. Liu, R. Guan, J. Magnes. Alloy. 13 (2025) 4299–4315, doi:10.1016/j.jma.2025.06.012.
[70] S. Zhu, M.A. Easton, T.B. Abbott, J.-F. Nie, M.S. Dargusch, N. Hort, M.A. Gibson, Metall. Mater. Trans. A 46 (2015) 3543–3554, doi:10.1007/s11661-015-2946-9.
[71] L. Feng, X. Dong, Q. Cai, B. Wang, S. Ji, J. Mater. Eng. Perform. 32 (2022) 2598–2606, doi:10.1007/s11665-022-06853-x.
[72] L. Feng, X. Dong, Q. Cai, B. Wang, S. Ji, J. Alloy. Compd. 923 (2022) 166364, doi:10.1016/j.jallcom.2022.166364.
[73] Y. Li, A. Zhang, C. Li, H. Xie, B. Jiang, Z. Dong, P. Jin, F. Pan, J. Mater. Res. Technol. 26 (2023) 2919–2940, doi:10.1016/j.jmrt.2023.08.055.

Please cite this article as: L. Feng, X. Dong, S. Wang et al., Tailoring microstructure and mechanical properties of high-pressure die-cast Mg-RE-Gd alloys via trace Al additions, Journal of Magnesium and Alloys, https://doi.org/10.1016/j.jma.2026.102023